


# Off-axis characterisation of the CERN T10 beam for low momentum proton measurements with a High Pressure Gas Time Projection Chamber

S.B. Jones<sup>10\*</sup> , T.S. Nonnenmacher<sup>3\*</sup>, E. Atkin<sup>3</sup>, G. J. Barker<sup>11</sup>, A. Basharina-Freshville<sup>10</sup>, C. Betancourt<sup>12</sup>, S. B. Boyd<sup>11</sup>, D. Brailsford<sup>5</sup>, Z. Chen-Wishart<sup>8</sup>, L. Cremonesi<sup>10</sup>, A. Deisting<sup>8</sup>, A. Dias<sup>8</sup>, P. Dunne<sup>3</sup>, J. Haigh<sup>11</sup>, P. Hamacher-Baumann<sup>9</sup>, A. Kaboth<sup>8</sup>, A. Korzenev<sup>2</sup>, W. Ma<sup>9</sup>, P. Mermod<sup>2</sup>, M. Mironova<sup>3,6</sup>, J. Monroe<sup>8</sup>, R. Nichol<sup>10</sup>, J. Nowak<sup>5</sup>, W. Parker<sup>8</sup>, H. Ritchie-Yates<sup>8</sup>, S. Roth<sup>9</sup>, R. Saakyan<sup>10</sup>, N. Serra<sup>12</sup>, Y. Shitov<sup>3,4</sup>, J. Steinmann<sup>9</sup>, A. Tarrant<sup>8</sup>, M. A. Uchida<sup>3,1</sup> S. Valder<sup>11</sup>, A. V. Waldron<sup>3</sup>, M. Ward<sup>8,7</sup>, M. O. Wascko<sup>3</sup>

<sup>1</sup> now at Cavendish Laboratory, Cambridge CB3 0HE, UK

<sup>2</sup> DPNC Université de Genève, 1205 Genf, Schweiz, CH;

<sup>3</sup> The Blackett Laboratory, Imperial College London, London SW7 2BW, UK;

<sup>4</sup> now at JINR, 141980 Dubna, RU

<sup>5</sup> Lancaster University, Bailrigg, Lancaster LA1 4YW, UK;

<sup>6</sup> now at Oxford University, Department of Physics, Oxford OX1 3PU, UK

<sup>7</sup> now at Queen's University, Kingston, Ontario, K7L 3N6, Canada

<sup>8</sup> Royal Holloway, University of London, Egham Hill, Egham, TW20 0EX, UK;

<sup>9</sup> RWTH Aachen University, III. Physikalisches Institut, 52056 Aachen, DE;

<sup>10</sup> University College London, Gower St, Kings Cross, London WC1E 6BT, UK;

<sup>11</sup> University of Warwick, Coventry CV4 7AL, UK;

<sup>12</sup> Physik-Institut, Universität Züriche, Rämistrasse 71, 8006 Zürich, CH;

\* Correspondence: sebastian.jones.17@ucl.ac.uk & toby.nonnenmacher14@imperial.ac.uk

Version 22nd July 2020 submitted to Instruments

1 **Keywords:** neutrino physics, time projection chamber, high pressure, CERN, beam test, time of flight,  
2 off axis

## 3 Abstract

4 We present studies of proton fluxes in the T10 beamline at CERN. A prototype high pressure gas  
5 time projection chamber was exposed to the beam of protons and other particles, using the 0.8 GeV/c  
6 momentum setting in T10, in order to make cross section measurements of low energy protons in argon.  
7 To explore the energy region comparable to hadrons produced by GeV-scale neutrino interactions at  
8 oscillation experiments, i.e. near 0.1 GeV of kinetic energy, methods of moderating the T10 beam were  
9 employed: the dual technique of moderating the beam with acrylic blocks and measuring scattered  
10 protons off the beam axis was used to decrease the kinetic energy of incident protons, as well as

11 change the proton/minimum ionising particle (MIP) composition of the incident flux. Measurements  
12 of the beam properties were made using time of flight systems upstream and downstream of the TPC.  
13 The kinetic energy of protons reaching the TPC was successfully changed from  $\sim 0.3$  GeV without  
14 moderator blocks to less than 0.1 GeV with four moderator blocks (40 cm path length). The flux of both  
15 protons and MIPs off the beam axis was increased. The ratio of protons to MIPs vary as a function  
16 of the off-axis angle allowing for possible optimisation of the detector to select the type of required  
17 particles. Simulation informed by the time of flight measurements show that with four moderator  
18 blocks placed in the beamline,  $(5.6 \pm 0.1)$  protons with energies below 0.1 GeV per spill traversed the  
19 active TPC region. Measurements of the beam composition and energy are presented.

## 20 1. Introduction

21 One of the major goals of the global neutrino physics programme is to explore fundamental  
22 symmetries of nature linked to why we live in a matter-dominated universe. Charge-parity symmetry  
23 violation (CPV) in the neutrino sector is one possibility remaining to be explored further experimentally,  
24 and neutrino experiments strive to improve current measurements of CPV in the leptonic sector [1].  
25 CPV is obtained from the simultaneous fit of the  $\nu_\mu$  disappearance and  $\nu_e$  appearance oscillation  
26 channels separately for neutrinos and anti-neutrinos. In the absence of CPV and accounting for matter  
27 effects, the rates of  $\nu_\mu \rightarrow \nu_e$  and  $\bar{\nu}_\mu \rightarrow \bar{\nu}_e$  oscillations should be equal. To convert the measured rate of  
28 interactions to a level of CPV, experiments must accurately know the cross section for the interactions  
29 of neutrinos and anti-neutrinos with detector materials, which are most commonly hydrogen, carbon,  
30 oxygen, argon, and iron. Therefore, systematic uncertainties on neutrino-nucleus interaction cross  
31 sections are a key input to such CPV searches. These interaction cross sections are dependent on  
32 modeling neutrino-nucleon interactions occurring within nuclei.

33 The nuclear models informed by these cross sections have substantial effects on the measured  
34 final-state particle kinematic distributions [2].

35 The long baseline neutrino experiments that are currently searching for CPV are the Tokai  
36 to Kamioka experiment (T2K) [1] and the NuMI Off-Axis  $\nu_e$  Appearance experiment (NOvA) [3].  
37 The T2K experiment, which currently reports the strongest constraint on CPV in neutrinos [1], has  
38 systematic uncertainties of 7-9% after near-detector constraint on the prediction of the rate of far  
39 detector electron-like events, with cross section uncertainties being the largest contribution. The  
40 future Deep Underground Neutrino Experiment (DUNE) [4] and Hyper-Kamiokande [5] projects  
41 will seek to reach 1-3% on that same rate of far detector electron-like events [6], with improved  
42 systematic errors providing better precision on the CP violating phase. The key to reducing these  
43 uncertainties is to precisely measure the multiplicity and momentum distribution of final-state particles.

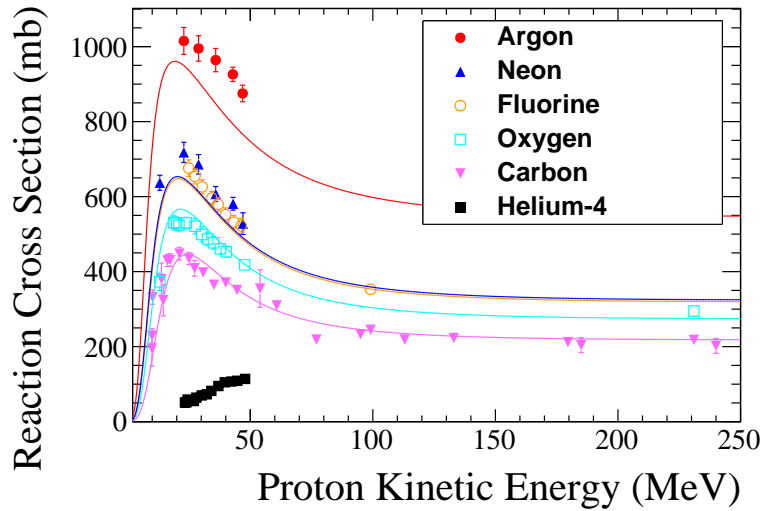


**Figure 1.** Total reaction cross sections for protons on argon, neon, fluorine, oxygen, carbon, and helium-4. Data [11] are compared to a semi-empirical model [12].

44 However, these distributions are modified by final state interactions (FSI) of the recoiling secondary  
 45 particles as they traverse the target nucleus. The most commonly used neutrino generator Monte  
 46 Carlos (GENIE [7], NEUT [8], and NuWro [9]), simulate FSI with cascade models that are tuned with  
 47 external hadron-nucleus scattering measurements. The generator GiBUU [10] models FSI by solving  
 48 the semi-classical Boltzmann-Uehling-Uhlenbeck equation.

49 However, as shown in Figure 1, proton-nucleus scattering measurements are extremely sparse  
 50 and in many cases do not exist in the relevant energy region and/or on the relevant nuclei. Therefore  
 51 semi-empirical parameterisations are used to extrapolate in momentum and atomic mass [12]. The  
 52 parameterisations are different between the three generators, and yield order-of-magnitude scale  
 53 differences in the predicted multiplicity and kinematics of final state protons [13]. The proton final  
 54 state modeling is a key ingredient for neutrino oscillation measurements because it affects the event  
 55 selection and neutrino energy reconstruction in charged-current (CC) interactions, which is the channel  
 56 used to measure oscillation parameters and is therefore central to the search for CPV [14]. For these  
 57 reasons, FSI contribute substantially to the total neutrino interaction systematic uncertainty [1].

58 Moreover, FSI models are in tension with data. Recent neutrino scattering measurements have  
 59 shown that the most-used models of neutrino-nucleus interactions (employed by NEUT and GENIE)  
 60 differ from nature in both cross section and kinematics of final state particles by as much as 30% [15].  
 61 These uncertainties cannot be fully mitigated with near/far detector combinations because they come  
 62 from theoretical model deficiencies that are not cancelled in the near–far extrapolation [16].

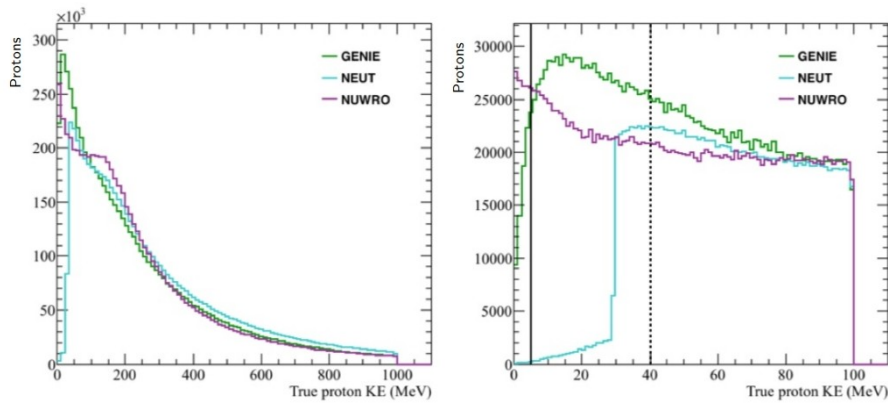


**Figure 2.** Predicted proton kinetic energy (KE) spectra from GENIE, NEUT, and NuWro [17]. Energy spectra up to 1 GeV are shown on the left, and zoomed in to lower energies on the right. The figure uses the Long Baseline Neutrino Facility (LBNF) simulation for DUNE’s beam energy and flux. The LBNF beam has a mean energy of approximately 2.5 GeV [4]. The dashed vertical line indicates the expected proton automated-reconstruction/identification threshold in liquid argon, and the solid vertical line shows the same for gaseous argon at 10 atm [13].

63 The key proton kinetic energy range in which to distinguish interaction models is the region  
 64 below 0.1 GeV. Figure 2 shows the proton multiplicity and kinetic energy distributions for  $\nu_\mu$  CC  
 65 interactions on argon calculated by the GENIE, NEUT, and NuWro neutrino generators for the DUNE  
 66 experiment. These distributions are highly discrepant at low proton kinetic energy as shown in the  
 67 right hand panel. The generators are not designed to handle the low energy region consistently, due  
 68 to the lack of available data. This is predominantly below the proton detection threshold in liquid  
 69 Argon TPCs (0.04 GeV), such as those that will be used by DUNE, and in water Cherenkov detectors  
 70 (0.5 GeV). The lower threshold in high pressure gas provides a unique opportunity to distinguish  
 71 between neutrino interaction models for the same nuclear target.

72 We have built a High Pressure gas Time Projection Chamber (HPTPC) prototype and exposed  
 73 it to a charged particle beam in the T10 beamline at CERN in August and September 2018 [18]. The  
 74 momentum profile of the T10 beam can be tuned within the range 0.8–6.5 GeV/c (kinetic energy range  
 75 0.3–5.6 GeV). Figure 3, left, shows the time of flight (ToF) spectrum for the T10 beamline tuned to a  
 76 momentum of 0.8 GeV/c; this measurement was made with our upstream ToF system (see Section 2  
 77 for details of the ToF systems). The kinetic energy of the protons calculated from the upstream ToF  
 78 measurements in this sample is shown in Figure 3, right. As shown, the flux of protons with kinetic  
 79 energy less than 200 MeV is negligible. The physics objective of the HPTPC beam test was to make  
 80 measurements of protons on argon at kinetic energies below 200 MeV, i.e. below what was available  
 81 with the T10 beam. Furthermore, the readout speed of the charge-coupled device cameras (CCD)  
 82 employed in the HPTPC prototype motivates a limit on the total particle multiplicity in the TPC active  
 83 volume.



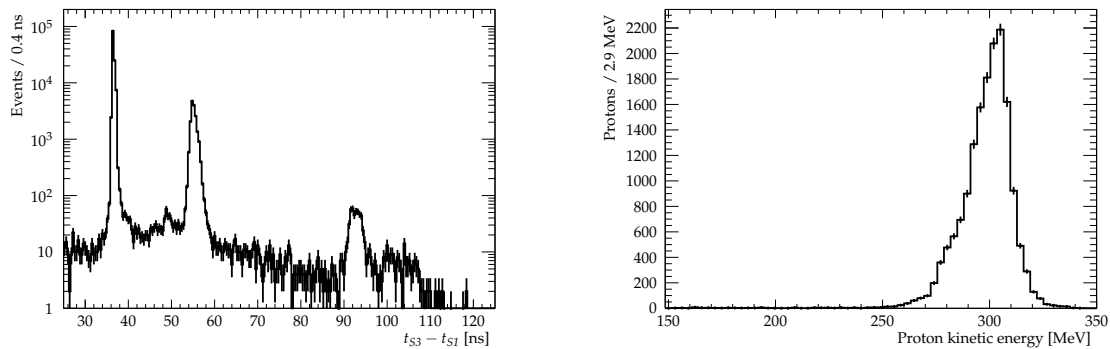


**Figure 3.** Measurements of the unmoderated and unbent T10 beam over a baseline of 10.8 m for a selected beam momentum of 0.8 GeV/c. Measurements are made in the S3 detector. The peak between 50 ns and 60 ns is produced by protons. Left: Time of flight spectrum. Right: Measured kinetic energy of protons.

84 To enhance the low energy proton flux, a novel technique was employed: we placed acrylic  
 85 moderator blocks directly in the beamline, which spread and slowed the beam particles via multiple  
 86 Coulomb scattering. By placing the TPC in an off-axis position with respect to the beam direction, we  
 87 observed a beam composition with lower-energy protons than would otherwise have been possible in  
 88 the T10 beamline. These techniques were designed to increase the ratio of protons to MIPs in the TPC,  
 89 and to decrease the proton momentum and multiplicity in the active region of the TPC.

90 The flux and composition of beam particles were measured with two ToF systems, placed  
 91 upstream and downstream of the TPC. Measurements of protons and MIPs are presented as a function  
 92 of the off-axis angle and thickness of the moderator. This paper provides a detailed description of the  
 93 time of flight systems employed in the beamline in Section 2, the analysis methodology of the ToF  
 94 data in Section 3, presentation of the ToF system results in Section 4, and additional conclusions in  
 95 Section 5.

## 96 2. Beam Line and Detectors

### 97 2.1. Beam Test Overview

98 The beam test took place in the T10 beam line, in the East Area at the Proton Synchrotron (PS)  
 99 at CERN. The T10 beamline at CERN is a secondary beam derived from the PS beam which consists  
 100 primarily of protons, electrons and charged pions [19]. The theoretical beam composition as a function  
 101 of beam momentum is shown in Figure 4. The primary components of the experimental setup are  
 102 shown schematically in Figure 5.

103 A beam position monitor (BPM) was situated at the beam entrance into the test area, upstream  
 104 of all the ToF constituents and the TPC. The TPC was placed 13 m downstream of the BPM. From  
 105 initial GEANT4 [20] beam simulations, the optimal TPC position to reduce the momentum of particles

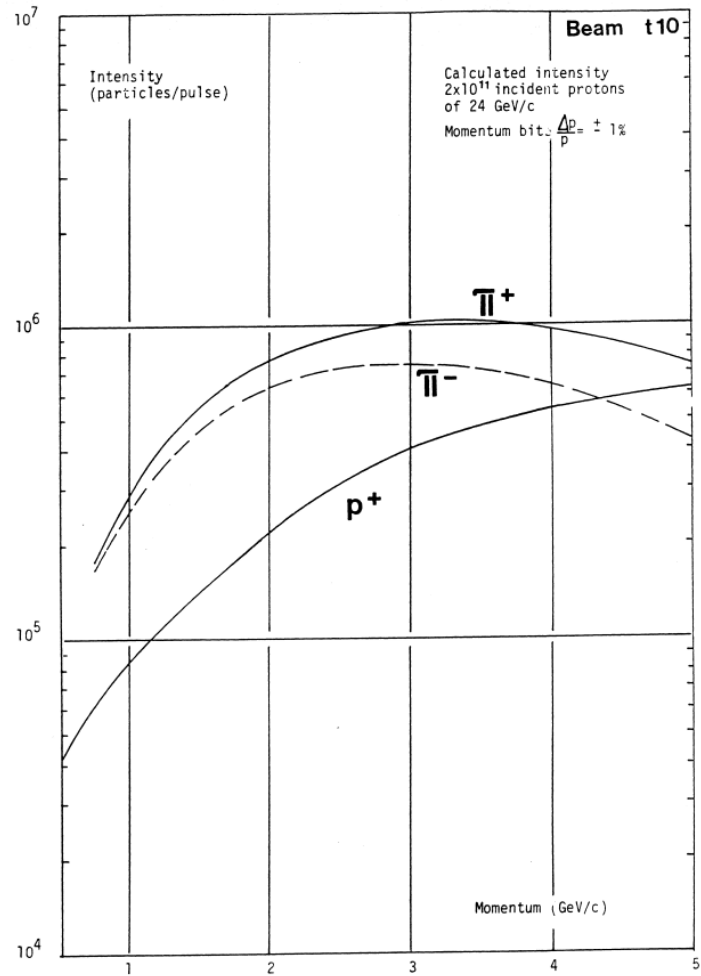


**Figure 4.** Calculated intensity of the T10 beam as a function of selected beam momentum, separated by particle type [19].

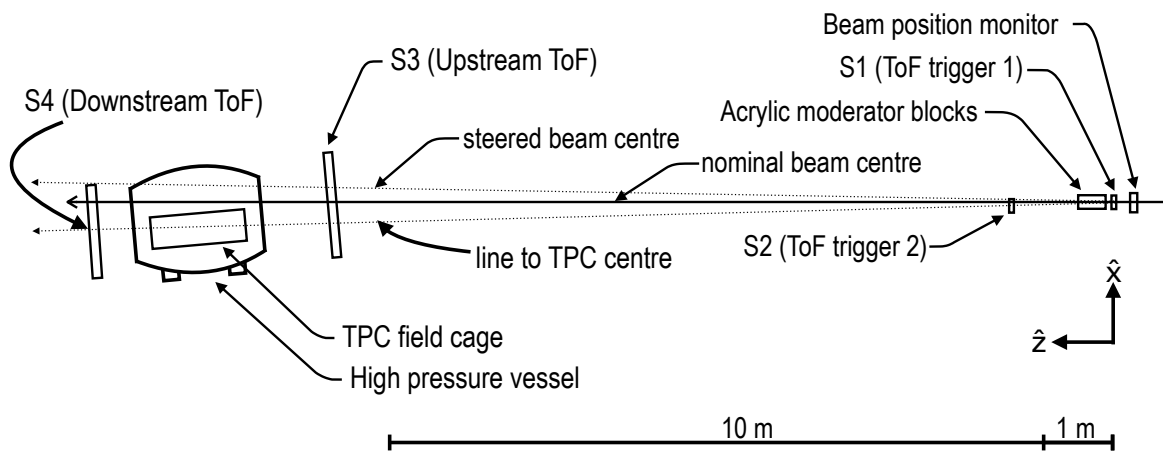


**Figure 5.** Schematic diagram (plan view) of the HPTPC beam test configuration in the T10 area at CERN.

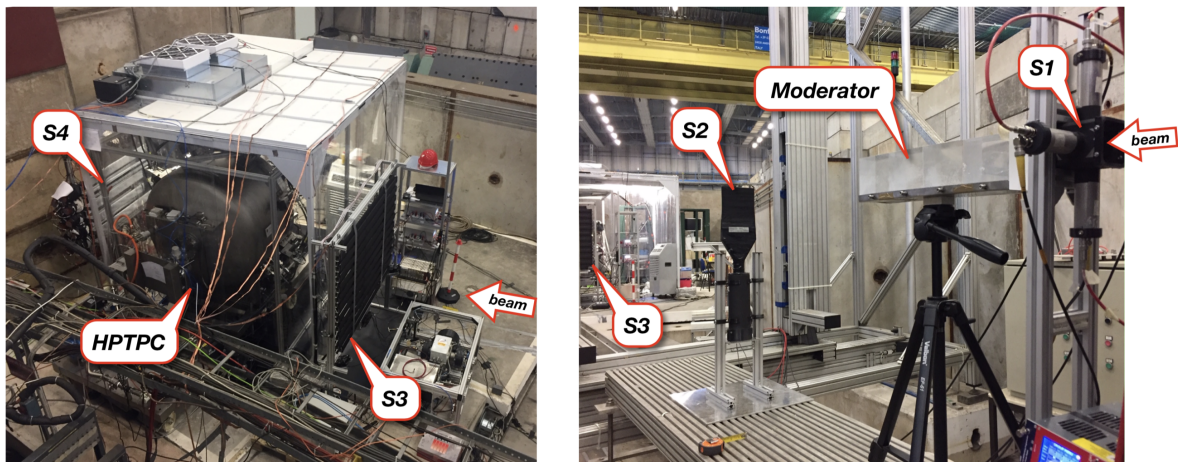


**Figure 6.** Photos illustrating the ToF constituents. Left: the downstream part of the setup which shows the *S3*, *S4* detectors and HPTPC. Right: *S1* and *S2* counters and the stand with four acrylic moderator blocks.

106 reaching the detector, without excessively reducing particle flux, was determined to be between  $2^\circ$   
 107 and  $3^\circ$  off the beam axis, but space constraints meant the TPC could not be placed that far away from  
 108 the nominal beam centre. So, the beam was steered approximately  $1^\circ$  away from its nominal position,  
 109 and the TPC placed  $1.5^\circ$  away from the nominal beam centre so that the TPC active region subtended  
 110 an off-axis angular range of  $1.4\text{--}3.8^\circ$ .

111 There were four ToF constituents:

- 112 • *S1*, a small-area beam trigger, see Section 2.3;
- 113 • *S2*, a coincidence measurement with *S1*, see Section 2.3;
- 114 • *S3*, a panel of plastic scintillator bars placed directly upstream of the TPC vessel, see Section 2.4;
- 115 • *S4*, a panel of plastic scintillator bars placed directly downstream of the TPC vessel, see  
 116 Section 2.5.

117 A series of acrylic (polymethyl methacrylate) blocks was placed between the *S1* and *S2* counters.  
 118 Up to four  $10 \times 10 \times 10 \text{ cm}^3$  acrylic blocks could be placed contiguously on a tripod stand. Figure 6  
 119 shows the stand with four blocks installed. The moderator blocks have the effect of both reducing  
 120 the energies of incoming particles as well as changing their directions. This tends to increase the  
 121 proton-to-MIP ratio at low off-axis angles from the beam, while decreasing the total number of protons  
 122 and MIPs traversing the TPC. Data were collected with the T10 beam momentum setting at  $0.8 \text{ GeV}/c$ ,  
 123 and with each configuration of 0 to 4 moderator blocks.

124 The data acquisition (DAQ) systems of the *S3* (upstream) and *S4* (downstream) ToF systems were  
 125 completely independent. Synchronization between ToF DAQ systems was performed offline using the  
 126 reference signal from the PS at the beginning of every spill. T10 received 1–3 spills from the PS during  
 127 each supercycle, which has a typical duration of 33 s. The spill duration is 400 ms. The minimum

128 separation in time between two spills is 1 second, so the start-of-spill signal frequency is less than or  
 129 equal to 1 Hz. Because of the low frequency of start-of-spill signal it is possible to use it, along with  
 130 the DAQ file timestamps, to ensure that all spills are matched in both DAQs. The trigger condition of  
 131 the upstream ToF was based on the coincidence between *S1* and *S3* constituents. *S2* signals were also  
 132 recorded by the upstream ToF DAQ but were not used in the trigger. The DAQ of the downstream  
 133 ToF was run in self-triggering mode with a gate open during the spill. Coincidence signals between  
 134 *S1* and *S2* counters were also recorded by the downstream ToF DAQ and were used in the particle  
 135 identification (PID) analysis, described in Section 4.

## 136 2.2. Survey and coordinate system

137 The T10 beamline area was surveyed, and the distances to specific components measured with a  
 138 precision of 0.5 mm by the CERN Survey, Mechatronics and Measurements (SMM) group. Multiple  
 139 points on each of *S1*, *S2*, *S3*, *S4* and the TPC frame have had their positions measured.

140 The axes of a right-handed coordinate system are defined as follows:  $\hat{x}$  refers to the non-beam  
 141 horizontal direction,  $\hat{y}$  to the vertical direction, and  $\hat{z}$  the beam direction, as shown in Figure 5. We  
 142 show results in terms of two off-axis angles:  $\theta$ , which is measured in the  $\hat{x} - \hat{z}$  plane with positive  
 143 angles measured in the  $+\hat{x}$  direction, and  $\phi$ , which is measured in the  $\hat{y} - \hat{z}$  plane with positive angles  
 144 measured in the  $+\hat{y}$  direction. The origin is taken to be at *S1*.

145 Figure 7 shows the angular extent of objects within the beamline using the coordinate system  
 146 defined above. Table 1 shows the calculated angular extent of the various beamline components as  
 147 measured from *S1*. Table 2 shows the distances between the centres of various objects in the T10  
 148 beamline. These distances were calculated using the data gathered by the survey team.

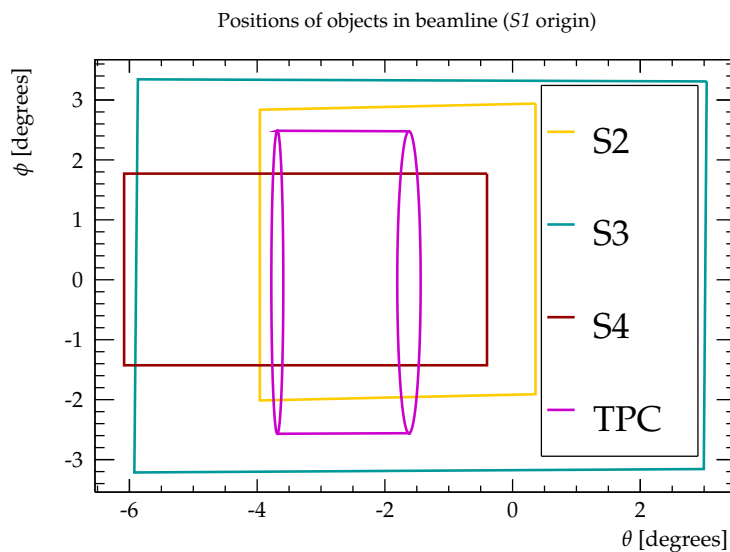


**Figure 7.** Angular position of various objects within the T10 beamline. The origin in this view is at the centre of *S1*; the true centre of the steered beam is at  $+1^\circ$  in  $\theta$  and  $0^\circ$  in  $\phi$ .

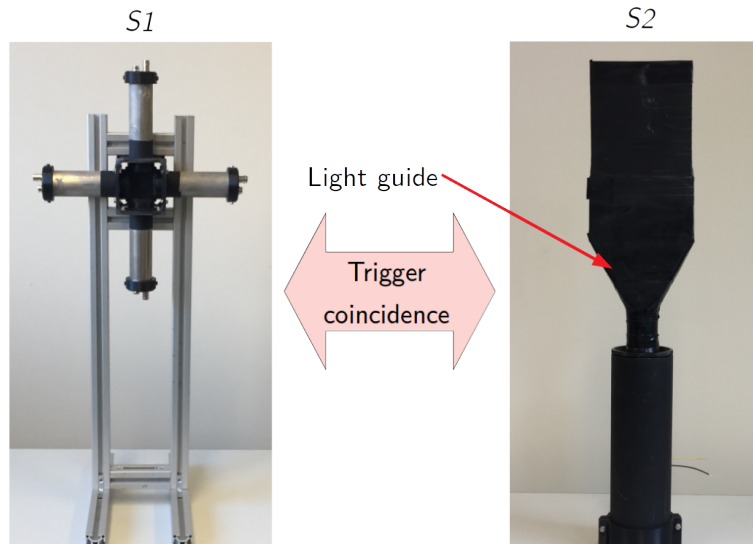
**Table 1.** Angular extents of objects within the T10 beamline as measured from *S1*.

Object	Minimum $\theta$	Maximum $\theta$	Minimum $\phi$	Maximum $\phi$
<i>S2</i>	$-3.96^\circ \pm 0.03^\circ$	$0.36^\circ \pm 0.03^\circ$	$-2.01^\circ \pm 0.03^\circ$	$2.94^\circ \pm 0.03^\circ$
<i>S3</i>	$-5.923^\circ \pm 0.004^\circ$	$3.040^\circ \pm 0.004^\circ$	$-3.215^\circ \pm 0.004^\circ$	$3.344^\circ \pm 0.004^\circ$
<i>S4</i>	$-6.083^\circ \pm 0.003^\circ$	$-0.401^\circ \pm 0.003^\circ$	$-1.426^\circ \pm 0.003^\circ$	$1.771^\circ \pm 0.003^\circ$
TPC upstream face	$-3.59^\circ \pm 0.01^\circ$	$-1.44^\circ \pm 0.01^\circ$	$-2.66^\circ \pm 0.01^\circ$	$2.58^\circ \pm 0.01^\circ$
TPC downstream face	$-3.778^\circ \pm 0.009^\circ$	$-1.806^\circ \pm 0.009^\circ$	$-2.440^\circ \pm 0.009^\circ$	$2.361^\circ \pm 0.009^\circ$

**Table 2.** Distances between objects in the T10 beamline. US and DS refer to the upstream and downstream edges of the TPC, respectively.

Points	Distance between centres / m
Beam monitor – <i>S1</i>	$0.288 \pm 0.001$
<i>S1</i> – <i>S2</i>	$1.419 \pm 0.001$
<i>S1</i> – <i>S3</i>	$10.756 \pm 0.001$
<i>S3</i> – TPC US side	$1.323 \pm 0.002$
TPC DS side – <i>S4</i>	$0.918 \pm 0.002$
<i>S2</i> – <i>S4</i>	$12.651 \pm 0.001$

### 149 2.3. Upstream beam counters (*S1* and *S2*)

**Figure 8.** The *S1* and *S2* beam counters. Together the coincidence of signals in the beam counters were recorded by the DAQ systems.

150 The beam counters *S1* and *S2* are shown in Figure 8. The *S1* counter is a  $40 \times 40 \times 5 \text{ mm}^3$  plastic  
 151 scintillator cross which is attached to four 1" Hamamatsu Photonics R4998 photomultiplier tubes  
 152 (PMTs) at each end for the light readout. The time resolution of the counter, as measured by the DAQ  
 153 system of the upstream ToF, was about 30 ps. This is estimated with the distribution of the average  
 154 PMT hit times; the quantity  $t_{\text{ave}} = \frac{1}{4}((t_{\text{PMT0}} + t_{\text{PMT1}}) - (t_{\text{PMT2}} + t_{\text{PMT3}}))$  has the same spread as the  
 155 simple average but is conveniently centered at zero. An example of the  $t_{\text{ave}}$  distribution for one run of  
 156 *S1* data is shown in Figure 9. The full width at half maximum (FWHM) of the distribution is 62 ps.

157 The *S2* counter is a scintillator tile of size  $120 \times 120 \times 5 \text{ mm}^3$ , coupled to a 2" Hamamatsu  
 158 Photonics R1309 PMT [21], via a long light-guide as shown in Figure 6. The *S2* counter was placed

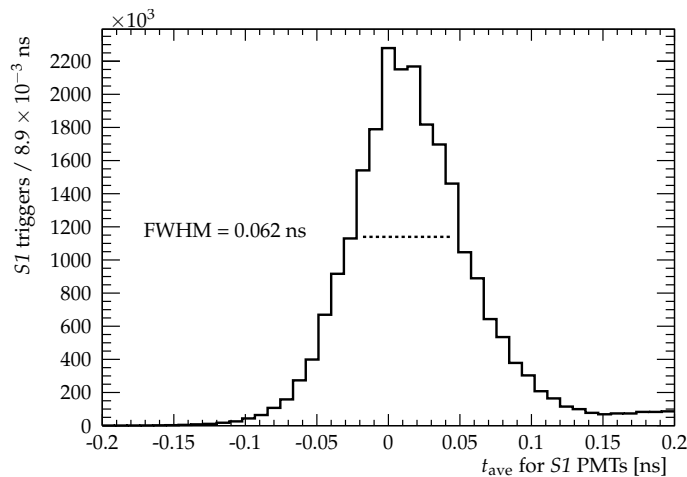


**Figure 9.** Example of the timing spread of *S1* hits. The time is calculated as an average of the hit time as measured in each of the four PMTs.

159 (1.419 ± 0.001) m downstream of *S1*. The transverse position of *S2* was adjusted to account for the  
 160 beam divergence in the moderator blocks.

161 The analog signals from one of the *S1* PMTs and the *S2* PMT were fed into LeCroy 620AL NIM  
 162 discriminator units with a threshold of 30 mV. Subsequently, the discriminated signals were fed into a  
 163 NIM coincidence unit, whose output was recorded by the DAQ systems of the downstream ToF (*S4*)  
 164 panel. This information was further used for the time-of-flight analysis of *S4*.

#### 165 2.4. Upstream Time of Flight instrumentation (*S3*)

166 The *S3* ‘upstream’ ToF constituent was placed (1.323 ± 0.001) m upstream of the upstream side  
 167 of the HPTPC drift volume in the beamline. A schematic drawing of the *S3* ToF panel is shown  
 168 in Figure 10, left. The detector comprises 22 staggered scintillator bars: 20 bars with dimensions  
 169 168 × 6.0 × 1.0 cm<sup>3</sup> and 2 bars of 150 × 6.0 × 1.0 cm<sup>3</sup> placed on top and bottom [22]. The overlap  
 170 between bars was set to 5 mm, thus the active area of the detector was 2.0214 cm<sup>2</sup>.

171 The bars are made from EJ-200 [23] plastic scintillator, which provides a brightness of  
 172 10,000 photons/MeV deposited. It also has a suitable optical attenuation length of 4 m and fast  
 173 timing, with a rise time of 0.9 ns and decay time constant of 2.1 ns. The scintillation emission spectrum  
 174 of EJ-200 peaks in the violet region of the visible spectrum (435 nm) [24]. The bars were wrapped in an  
 175 aluminium foil (60% reflectivity) to increase the collected light.

176 Arrays of eight 6 × 6 mm<sup>2</sup> area silicon photomultipliers (SiPMs) S13360-6050PE from Hamamatsu  
 177 Photonics [21] were coupled to each end of the bar to collect scintillation photons. The photon detection  
 178 efficiency at the peak sensitivity wavelength (450 nm) is 40% [21]. The anode signals of the SiPMs are  
 179 read out, summed and shaped by a dedicated circuit as described in Ref. [25].

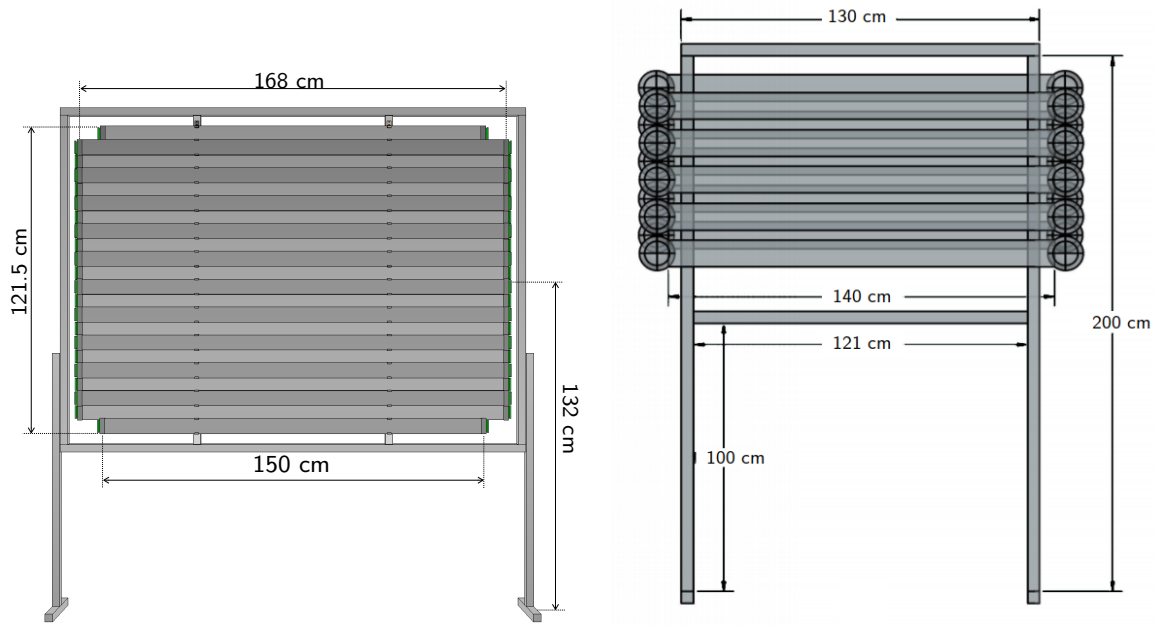


**Figure 10.** View of the time of flight panels. Left: The S3 panel [22] upstream of the TPC. Right: The S4 panel downstream of the TPC.

180 S3 uses a 64 channel data acquisition system based on the SAMPIC chip. A SAMPIC chip is a  
 181 waveform and time to digital converter (WTDC) 16-channel ASIC which provides a raw time with  
 182 ultrafast analog memory allowing fine timing extraction as well as other parameters of the pulse [26].  
 183 Each channel contains a discriminator that can trigger itself independently or participate in a more  
 184 complex combined trigger. Three ASIC modules ( $16 \times 3 = 48$  channels) were connected to the 44  
 185 channels of S3 and were operated in self-triggering mode.

186 The trigger conditions are as follows: at least three out of the four S1 PMTs must have a signal  
 187 above a 30 mV threshold. Additionally, there must be at least one signal in S3 above 30 mV. These  
 188 S1 and S3 signals must be coincident within a gate of 70 ns. A fourth ASIC was used to acquire data  
 189 from S1, the coincidence signal  $S1 \cap S2$ , and the start-of-spill signal from the PS. The mean time of  
 190 light signals detected at both ends of a single bar provides a time reference with a resolution of about  
 191 100 ps, while the difference between the time of the light signals gives the position of the interaction  
 192 along the bar, with a resolution of 1.6 cm.

193 Examples of reconstructed S3 spatial distributions are shown in Figure 11. Figure 11, left, shows  
 194 the spatial distribution of hits in S3 thought to be produced by MIPs when 4 moderator blocks were  
 195 in the beamline. Figure 11, right, shows the spatial distribution of hits identified in S3 as protons  
 196 when 4 moderator blocks were in the beamline. The pattern of hits is more diffuse, illustrating the  
 197 scattering effect of the moderator blocks. When in this position, the measured horizontal FWHM of  
 198 the unmoderated beam is 16.8 cm while the vertical FWHM is 11.0 cm. With 4 moderator blocks in the  
 199 beamline, the measured horizontal FWHM of the beam is 63.8 cm while the vertical FWHM is 60.0 cm.



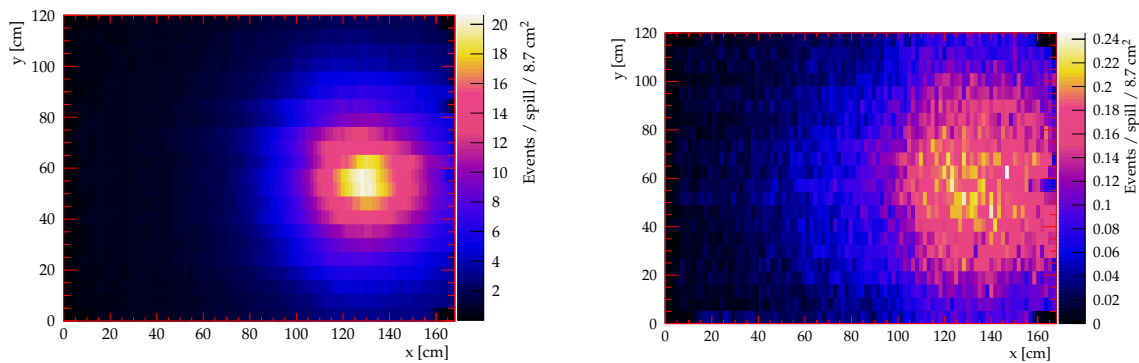


**Figure 11.** Reconstructed positions of hits observed in S3. Left: minimum ionizing particles with four moderator blocks placed in the beamline. Right: protons detected with four moderator blocks placed in the beamline. This figure uses local S3 coordinates in which  $y, x = 0$  cm is the bottom right corner of the active area when viewed from S1.

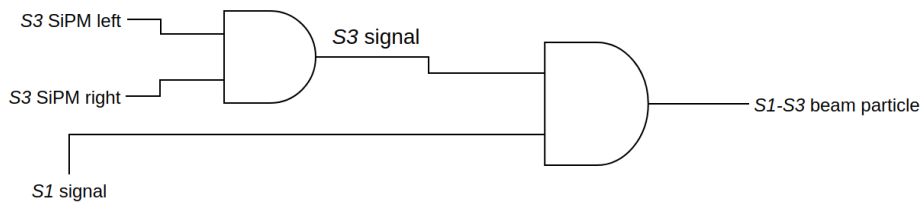


**Figure 12.** Simplified trigger logic diagram for the upstream ToF detection of a beam particle, showing the required coincidences. Left and right refer to the SiPMs on the opposite ends of the same bar.

200 Figure 12 shows the required trigger logic for the detection of a beam particle in the upstream ToF  
 201 instrumentation. The signal thresholds and timing cuts used for the coincidences are those detailed in  
 202 this section.

### 203 2.5. Downstream Time of Flight instrumentation (S4)

204 The S4 'downstream' ToF constituent sat ( $0.918 \pm 0.001$ ) m downstream of the downstream edge  
 205 of the drift volume of the HPTPC prototype in the beamline. It consists of 10 bars of Nuvia NuDET  
 206 plastic scintillator which has a wavelength of maximum emission of 425 nm and a decay time constant  
 207 of 2.5 ns [27]. Each of these bars measure  $10 \times 1 \times 140$  cm<sup>3</sup>. Attached to each end of these scintillator  
 208 bars is a 5" Hamamatsu Photonics R6594 PMT [21]. The bars are arranged in two rows of five, such that  
 209 there is complete coverage for any beam particles incident upon the detector. The bars are wrapped  
 210 individually in reflective milar sheets to increase the light yield. The total active area of the S4 panel is  
 211  $1.40 \times 0.78$  m<sup>2</sup>. A diagram of S4 along with its dimensions is presented in Figure 10, right.

212 The time resolution of the bars and PMTs is measured to be 0.8 ns using a <sup>90</sup>Sr source placed at  
 213 measured distances along the bar. Figure 13 is the measured time difference for signals coming from  
 214 the PMTs at either end of a bar caused by the <sup>90</sup>Sr at a given position. Figure 13 shows an example of

215 the distribution from which the time resolution was derived. The corresponding spatial resolution of  
 216 the bars and PMTs was measured to be 7 cm.

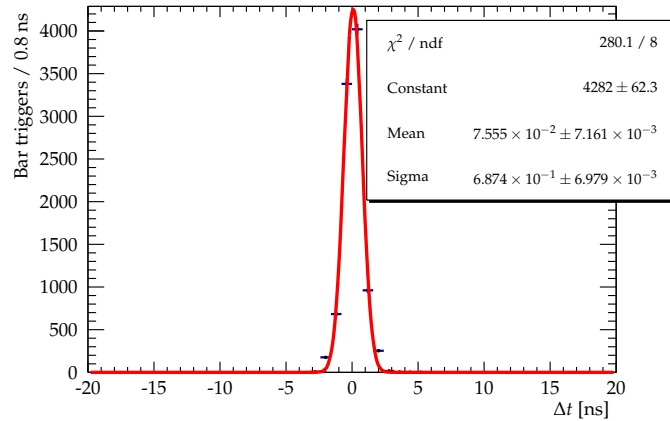


**Figure 13.** Difference in signal arrival time for PMTs at each end of a bar as measured using a  $^{90}\text{Sr}$  source placed 64 cm from one end of the bar.

217 The anode signals of all 20 of the PMTs are discriminated using LeCroy 620AL NIM discriminators,  
 218 at a threshold of 20 mV. The discriminated signals are then fed into a time-to-digital converter (TDC).  
 219 A signal in *S4* is deemed to have occurred if a signal is seen in both PMTs, above the discriminator  
 220 threshold, on the same bar within 20 ns of each other. This timing window is determined through  
 221 testing performed with a  $^{90}\text{Sr}$  source at known positions on the bar.

222 The *S1* – *S2* coincidence signal is digitized by the same TDC. This signal is used to calculate the  
 223 particle time of flight from *S2* to *S4*.

## 224 2.6. The HPTPC Prototype

225 For the characterisation of the beam using the ToF systems described in this paper, the relevant  
 226 characteristics of the HPTPC prototype are the location and thickness of the steel vessel walls. The  
 227 cylindrical steel vessel has a 142 cm outer diameter; the main body is 60 cm in length and the rounded  
 228 end caps protrude an additional 37 cm on each end. With 1 cm thick walls it is rated to 6 bar of absolute  
 229 pressure. The vessel wall thickness is equivalent to the range of a proton with a kinetic energy of  
 230 approximately 80 MeV [28]. For the unmoderated beam, the typical energy loss of a proton which  
 231 does not stop in the vessel is 50 MeV. This is determined from the Monte Carlo studies detailed in  
 232 Section 4.3. The angular position of the center of the TPC is approximately  $\theta = -2.5^\circ$ . More details of  
 233 the position and extent of the TPC are given in Table 1 and Table 2.

234 The active TPC is a cylinder, 111 cm in diameter and 48 cm in length; the TPC comprised thin steel  
 235 mesh electrodes (one cathode with 118 cm diameter and three anodes with 121 cm diameter), and 12  
 236 copper rings to create the uniform drift field. The anodes were supported by a hexagonal aluminium

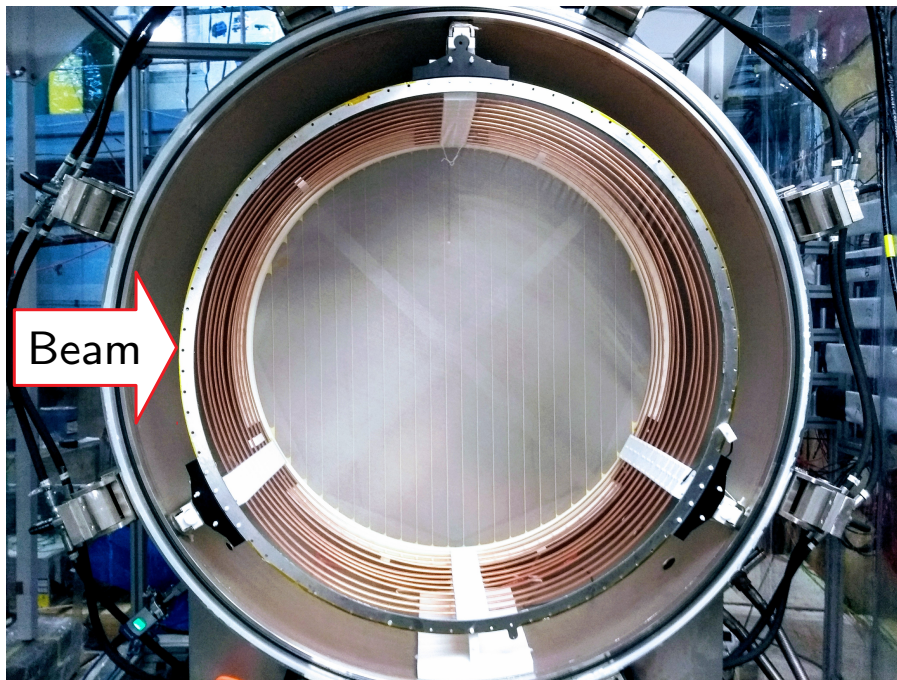


**Figure 14.** Cross-sectional view of the TPC; the thin mesh electrodes and copper ring drift volume can be seen inside the steel vessel. The walls of the vessel shown are 1 cm thick with a vessel outer diameter of 142 cm. At the point of hitting the vessel, the beam centre was 1 cm below the centre of the vessel vertically, where the distance from the inside of the vessel wall to the drift region was 15 cm.

237 stiffener on the side facing away from the camera. Data taking with the TPC made use of both optical  
238 and charge readout. The vessel, electrodes, and drift region of the TPC are shown in Figure 14.

239 Throughout the run, the TPC was filled with either pure argon, or a combination of argon  
240 and a small percentage of quencher. The performance of this TPC is the subject of a forthcoming  
241 publication [29].

### 242 3. Analysis

#### 243 3.1. Analysis Goals

244 The primary aim of this analysis are to assess the feasibility of using the combination of off-axis  
245 positioning and a moderated beam to produce particles with momenta covering the range of momenta  
246 of particles produced in GeV-scale neutrino interactions and to characterize the incident flux on the  
247 TPC and exiting the TPC, for the TPC data analysis.

248 The numbers of spills recorded for each number of moderator blocks are shown in Table 3. More  
249 data were collected for 4 blocks as that was the configuration used for the majority of the beam test.

**Table 3.** Total number of spills recorded for each moderator block configuration included in this paper.

Number of moderator blocks	Recorded spills
0	257
1	254
2	267
3	220
4	3884

### 3.2. Time of flight analysis

A charged pion with a momentum of 0.8 GeV/c will have a time of flight from  $S1$  to  $S3$  (a distance of 10.8 m) of 37 ns, while a proton with the same momentum will have a time of flight of 55 ns. For the same two particles travelling between  $S2$  and  $S4$  (a distance of 12.7 m), the charged pion would have a time of flight of 43 ns and the proton would have a time of flight of 65 ns. Figure 15, left and right, shows the predicted time of flight for various particle species across the  $S1 - S3$  distance and the  $S2 - S4$  distance respectively.

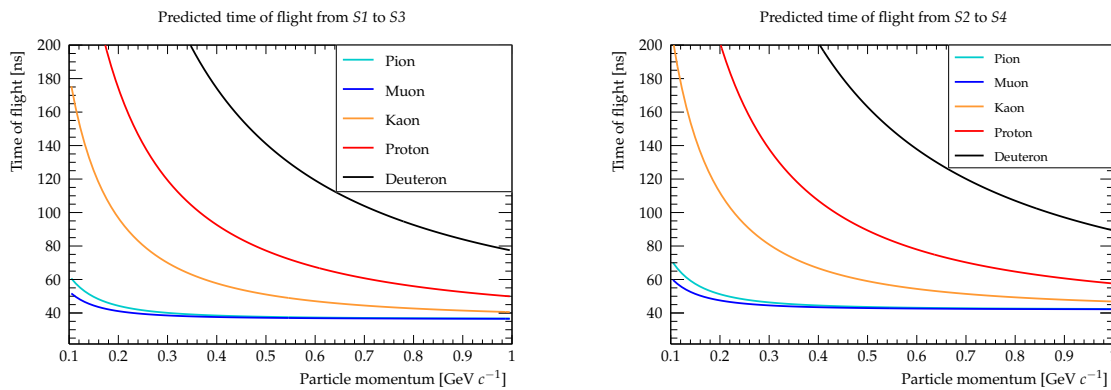
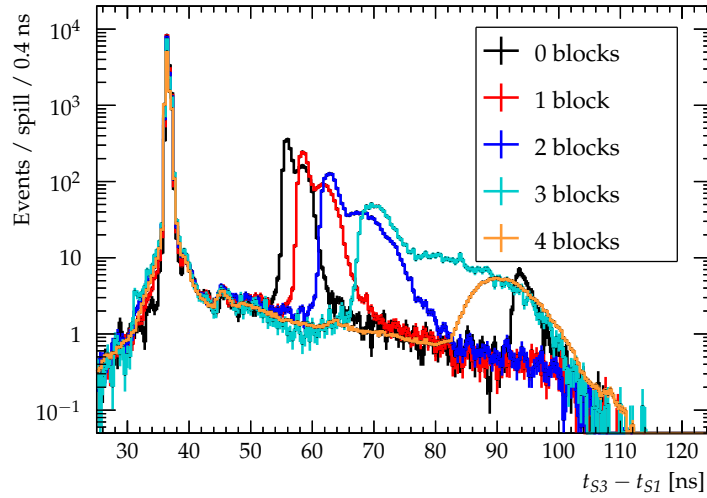
**Figure 15.** Calculated time of flight for a number of different particle species as a function of particle momentum. Left: ToF between  $S1$  and  $S3$ . Right: ToF between  $S2$  and  $S4$ .

Figure 16 shows the time of flight spectrum recorded in the  $S3$  timing point for varying numbers of moderator blocks. The quicker peak is formed by minimum ionizing particles, while the peak at higher values of  $t_{S3} - t_{S1}$  corresponds to protons. The proton peaks show a double peak feature, with a smaller delayed peak closely following the main proton peak; this feature appeared after the beam was steered so that the full 2.5 degree off-axis angle could be achieved and is due to a portion of beam scattering in the steering magnets, leading to the slower peak. The part of the beam which does not impinge on the steering magnets produces the quicker proton peak in the spectrum. Figure 3, left and right, shows the proton peak for unsteered beam and the double peak structure is gone. In the black curve, which shows the 0 block data, a deuteron peak can be seen centered at 95 ns. The timing ranges for particle species selection are chosen using the analytic expectations shown in Figure 15.

To calculate the correct time of flight, timing delays caused by cabling and equipment are taken into account. The same method is used to correct the measurements of the time of flight between  $S1$



**Figure 16.** S3 time of flight spectra for varying numbers of moderator blocks.

269 and S3, and S2 and S4. The initial recorded time,  $t_i$ , is either  $t_{S1}$  or  $t_{S2}$  while the final recorded time,  $t_f$   
 270 is then  $t_{S3}$  or  $t_{S4}$  respectively.

271 Timing offsets are measured in the beamline by assuming that the fastest peak in the  $t_f - t_i$   
 272 spectrum for the unmoderated data is produced by charged MIPs with a momentum of 0.8 GeV/c.  
 273 The required timing shift is then the shift required to move the fastest peak to its expected position,  
 274 given this assumption. This shift is then applied to all measured times of flight. This correction is  
 275 performed separately for both the measurement of  $t_{S3} - t_{S1}$  and for the measurement of  $t_{S4} - t_{S2}$ . The  
 276 required timing shift for the  $t_{S4} - t_{S2}$  measurement is 43.7 ns. For the  $t_{S3} - t_{S1}$  measurement, the  
 277 required timing shift is 65.0 ns.

278 The mass distribution calculated for the dataset without moderator blocks is shown in Figure 17.  
 279 The time difference between S3 and S1 counters corresponding to a single particle ( $t_{S3} - t_{S1}$ ) is  
 280 converted to the mass of the particle,  $m$ , using Equation 1, where the equation is in natural units. The  
 281 particle momentum,  $p$ , is assumed to be 0.8 GeV/c.

$$m^2 = p^2 \left( \left( \frac{t_{S3} - t_{S1}}{x_{S3} - x_{S1}} \right)^2 - 1 \right), \quad (1)$$

282 The proton and pion mass positions in Figure 17 are indicated by vertical arrows. One can clearly  
 283 observe distinct peaks corresponding to protons and deuterons. The insert in the figure shows a  
 284 zoomed region corresponding to the MIPs.

285 For the data collected in S3, both timing and signal amplitude cuts were used to select protons  
 286 and MIPs. Figure 18 shows an example of the signal size recorded in one of the SiPMs on one of the  
 287 scintillator bars against the measured value of  $t_{S3} - t_{S1}$ . At the beam energies used, due to their higher  
 288 mass, the protons typically deposit more energy in the detector, resulting in the observation of greater

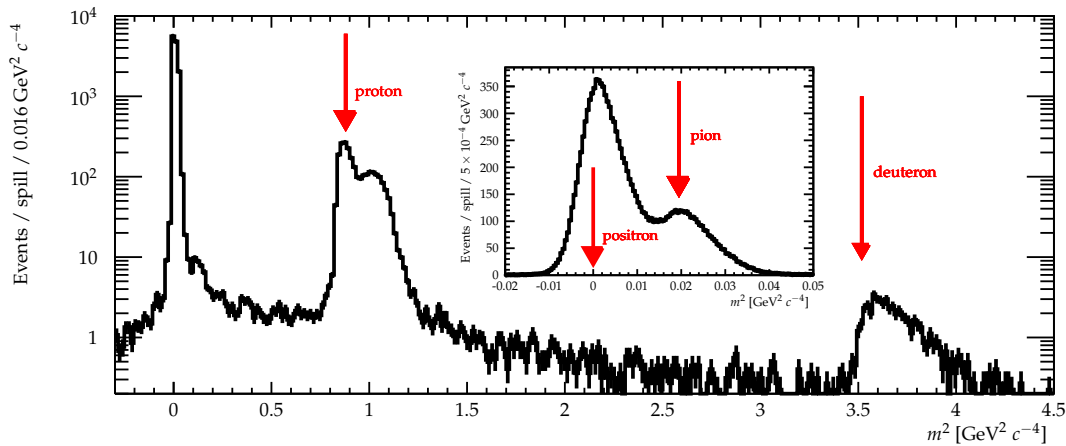


**Figure 17.** Reconstructed mass spectrum for the data taken without moderator blocks. The spectrum was calculated using the time difference between  $S3$  and  $S1$ . Vertical arrows show predicted position of particles given a momentum of  $0.8 \text{ GeV}/c$ . Insert: Zoomed view of MIP region of the same spectrum.

289 amplitudes. Therefore, to reduce the number of background events in the proton sample, a minimum  
 290 signal amplitude is required. This cut varies, depending on the SiPM in question and is determined  
 291 from distributions such as those shown in Figure 18. The cut values vary in the range  $0.125 \text{ V}$  to  $0.3 \text{ V}$ .

292 Particles for which  $35.75 \text{ ns} < t_{S3} - t_{S1} < 37.75 \text{ ns}$  are identified as MIPs. Particles which pass the  
 293 amplitude cut and for which  $53 \text{ ns} < t_{S3} - t_{S1} < 115 \text{ ns}$  are identified as protons. The upper bound of  
 294 this timing cut is reduced to  $80 \text{ ns}$  for the unmoderated sample in order to exclude deuterons.

295 A correction must be applied to the upstream ToF DAQ ( $S1$ ,  $S2$  and  $S3$ ) to account for its large  
 296 dead time. The  $S1 \cap S2$  signal is digitised by both the upstream and downstream ToF DAQ. The dead  
 297 time of the downstream ToF DAQ is found to be negligible. A linear relationship between the number  
 298 of  $S1 \cap S2$  signals measured in each DAQ is determined for each moderator block sample. Therefore,  
 299 events measured in the upstream ToF DAQ are weighted, such that the number of  $S1 \cap S2$  signals  
 300 measured in the upstream and downstream ToF DAQs are approximately equal.

301 Figure 19 shows the variation in the time of flight spectrum as recorded by  $S4$  with a changing  
 302 number of moderator blocks. This spectrum is given by the difference in time between observation of  
 303 a coincidence in the  $S1$  and  $S2$  timing points and a signal being recorded in  $S4$  (the definition of an  $S4$   
 304 signal is given above).

305 Additionally, the reconstructed mass distribution for particles travelling from  $S2$  to  $S4$  is shown in  
 306 Figure 20, produced using Equation 1. Unlike the same distribution produced for particles travelling  
 307 from  $S1$  to  $S3$  (see Figure 17), no deuteron peak is visible. This is thought to be due to the attenuation  
 308 of deuterons within the walls of the TPC. Additionally, the predicted proton position does not line up  
 309 with the measured proton position. This is again thought to be caused by the positioning of the TPC  
 310 in front of  $S4$ . Protons passing through the TPC lose energy, resulting in them having less than the



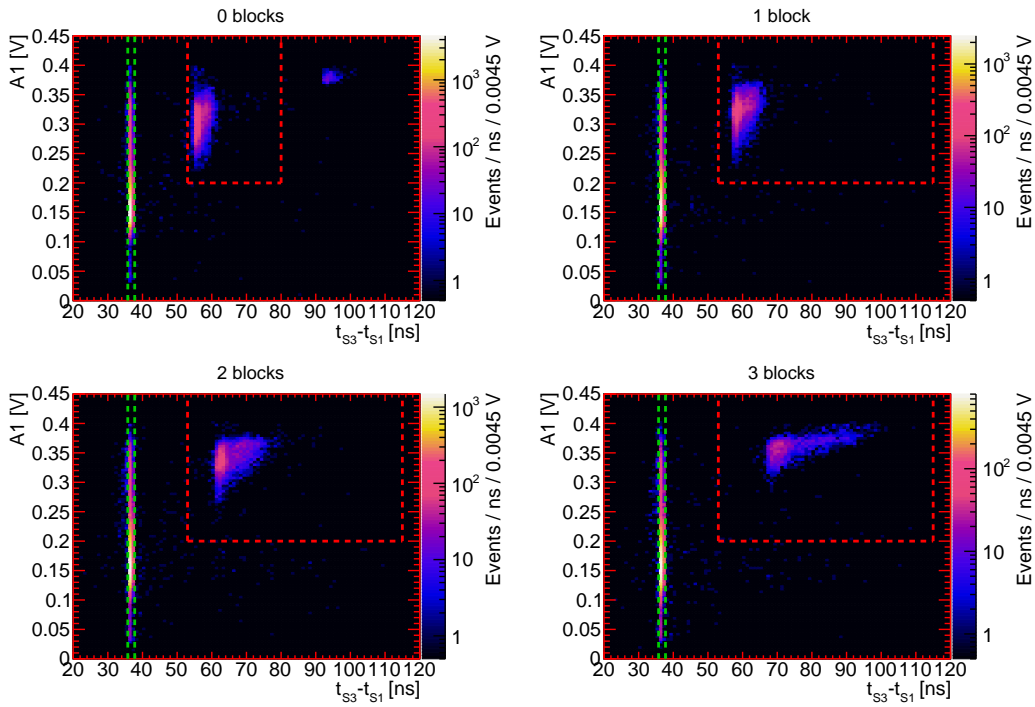


**Figure 18.** Examples of SiPM signal amplitude plotted against  $S1$  to  $S3$  time of flight for different numbers of moderator blocks. Clockwise from top left 0, 1, 3 and 2 moderator blocks are shown.  $A1$  is the voltage recorded in the SiPM at the end of the bar. The red horizontal dashed line shows the amplitude cut used for this particular SiPM. Events in the area enclosed by the red dashed lines are selected as protons. Events enclosed by the green dashed lines are selected as MIPs.

311 original 0.8 GeV/c beam momentum. In turn, this leads to protons having a larger reconstructed mass  
 312 than predicted. The displacement of the proton mass peak in Figure 20 is consistent with the expected  
 313 energy loss in the vessel walls. This consistency is shown with Monte Carlo studies in Section 4.3.  
 314 These Monte Carlo studies also show that, at the energies used in this study, approximately 40% of  
 315 protons which impinge on the vessel stop within it.

316 A correction is made for the variation in particle detection efficiency between the bars and for the  
 317 variation in this efficiency as a function of the position along each bar. This correction is performed  
 318 using the cosmic ray flux. It is assumed that the flux of cosmic rays passing through each part of  
 319  $S4$  is equal. Each  $S4$  bar is divided into 7 cm segments for analysis, and the number of cosmic rays  
 320 passing through each segment is measured by assuming that all signals occurring outside of beam  
 321 spills are produced by cosmic rays. The efficiency is then found from this distribution by normalising  
 322 the bin with the highest number of cosmic ray signals to 1. This efficiency is highest around the middle  
 323 of the bars (70 cm) because of the requirement that coincident signals are observed in both PMTs  
 324 on a given bar in order for a hit to be recorded. An example of one of these distributions is shown  
 325 in Figure 21. Events are then weighted according to the bar in which they are observed and their  
 326 measured position along this bar. The weight applied is the inverse of the value shown on the z-axis



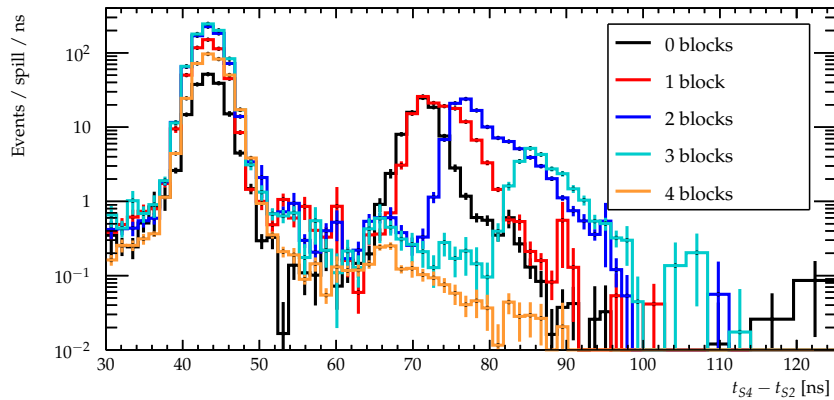


**Figure 19.**  $S_4$  time-of-flight spectra for varying numbers of moderator blocks. For all configurations, a flat background has been fitted and subtracted from the data. Additionally, the plot has also been corrected for the differing efficiencies of the various bars and for the variation in efficiency as a function of position along the bar, as described in Section 3.2.

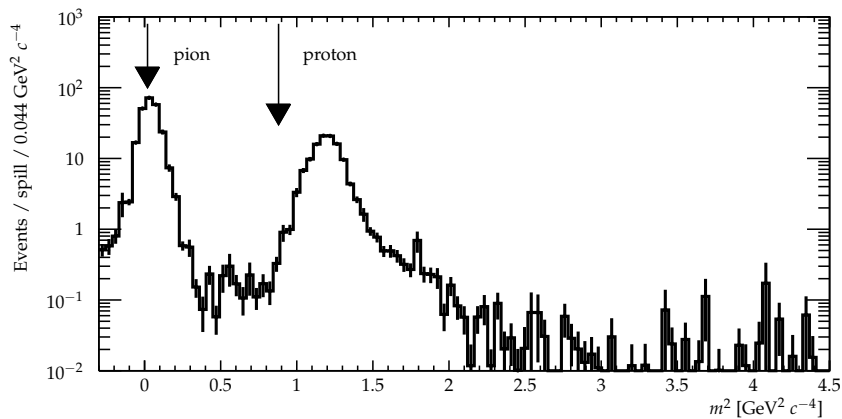


**Figure 20.** Reconstructed mass spectrum for the data taken without moderator blocks. The spectrum was calculated using the time difference between  $S_4$  and  $S_2$ . Vertical arrows show predicted position of particles.

327 of Figure 21. Additionally, a further weight is applied to all  $S_4$  events of 1.25. This weight is derived  
 328 from tests performed on the  $S_4$  bars with a  $^{90}\text{Sr}$  source. Using this source, it was determined that the  
 329 maximum measured rate of signals produced by the  $^{90}\text{Sr}$  source was equal to 0.8 of the true rate.

330 Using Figure 19, protons and MIPs are selected with timing cuts and a flat background is then  
 331 subtracted. The particles in the quicker timing window (those for which  $36 \text{ ns} < t_{S_4} - t_{S_2} < 51 \text{ ns}$ )  
 332 are considered to be minimum ionizing particles while those in the slower timing window (those for  
 333 which  $62 \text{ ns} < t_{S_4} - t_{S_2} < 125 \text{ ns}$ ) are considered to be protons.

334 The background is determined by fitting a sum of signal and background functions to the time of  
 335 flight spectra. The signal functions are taken to be Gaussians while the background is taken to be flat.  
 336 An example of this is shown in Figure 22. The background rates for each sample are shown in Table 4.  
 337 These backgrounds have been subtracted from the totals shown in Section 4.2.

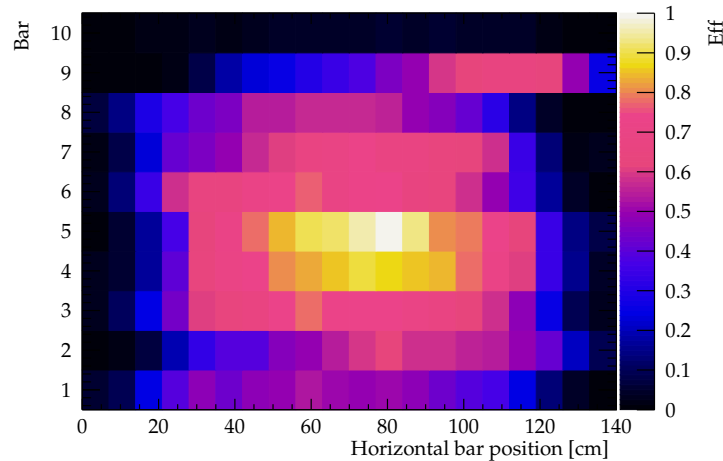


**Figure 21.** Relative detection efficiency of  $S4$  as a function of bar number and position along each bar as measured with cosmic rays. The data from bar 10 was not used in the analysis due to the poor efficiency along the bar.

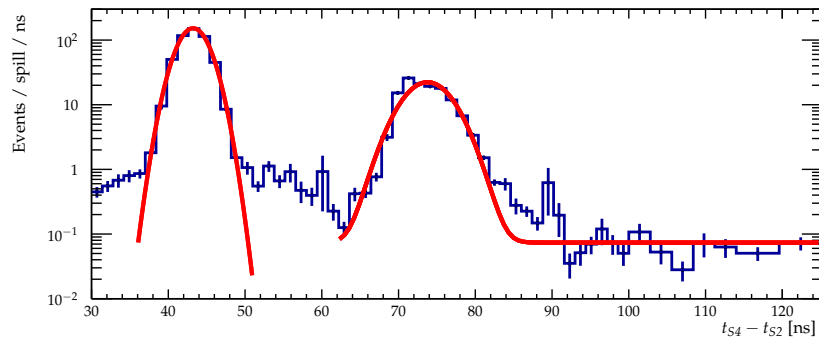


**Figure 22.** Example of the time of flight spectrum observed in  $S4$  with combined signal and background functions fitted (shown in red).

338 The backgrounds follow the same pattern as the total measured  $S4$  particle rates (see Section 4.2).  
 339 The background rate initially increases with the addition of the addition of more moderator blocks  
 340 then decreases for the 3 and 4 moderator block configurations.

341 The ratio of the rate of signal protons to the background rate falls with the addition of moderator  
 342 blocks. This is due to increased scattering from the moderator blocks which causes more particles to  
 343 strike  $S4$  without passing through  $S2$ . This leads to an increase in false coincidences which contribute  
 344 to the background rate.

#### 345 4. Beam Flux Measurement

##### 346 4.1. Flux measurements with $S3$

347 The ToF systems are at an off-axis angle with respect to the beam axis (see Table 1), in order  
 348 to probe the reduced proton momentum spectrum, to cover the region most relevant for neutrino

**Table 4.** Background rates for the time of flight spectra measured in *S4*. To convert these to the number of expected background events in a spill, the rate is multiplied by the size of the timing window for either MIPs or protons.

Number of moderator blocks	Background / Events $\times$ spill <sup>-1</sup> $\times$ ns <sup>-1</sup>
0	$0.037 \pm 0.004$
1	$0.066 \pm 0.005$
2	$0.165 \pm 0.007$
3	$0.124 \pm 0.009$
4	$0.085 \pm 0.002$

349 experiments and to measure the flux passing through the TPC. This is quantified in terms of  $\theta$  and  $\phi$   
 350 (see Section 2.2).

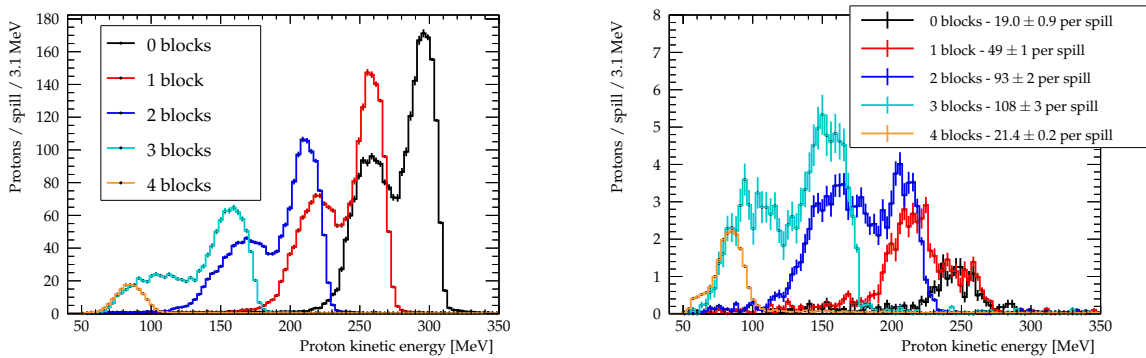


**Figure 23.** Proton kinetic energy spectrum as measured in *S3*. Left: all protons. Right: the subset of protons passing through the HPTPC drift volume. The errors shown in the legend are the statistical error in particle number per spill.

351 The proton spectra upstream of the TPC are shown in Figure 23. Figure 23, left, shows the kinetic  
 352 energy of particles identified as protons is successfully reduced with increasing numbers of moderator  
 353 blocks, with the range falling from 210-320 MeV for the unmoderated beam, to 60-110 MeV for 4 acrylic  
 354 blocks. Figure 23, right, shows the kinetic energy spectrum of protons crossing into the TPC. This  
 355 figure indicates that the flux of low energy protons (those with a kinetic energy of less than 80 MeV)  
 356 reaching the TPC was increased from negligible in the 0, 1, and 2 block cases to  $(9.7 \pm 0.1)$  per spill for  
 357 the 4 block case. Comparing Figure 23, right, with Figure 2 shows that, for the four moderator block  
 358 case, the kinetic energy of protons incident upon the TPC is just above the 50 MeV region where the  
 359 different neutrino interaction generators become discrepant. These protons lose further energy within  
 360 the walls of the HPTPC vessel, resulting in a flux of protons below 50 MeV within the TPC.

361 The combination of the use of moderator blocks and positioning the TPC in an off-axis position  
 362 also caused a change in the multiplicity of protons passing through the TPC. Figure 23, right, shows  
 363 that the addition of 1, 2, and 3 moderator blocks increased the number of protons passing through the  
 364 TPC from  $(19.0 \pm 0.9)$  per spill in the unmoderated case to  $(108 \pm 3)$  per spill in the 3 block case. The

365 addition of the fourth moderator block effectively removes the flux of protons above 100 MeV, leaving  
 366  $(21.4 \pm 0.2)$  per spill to traverse the TPC active volume.

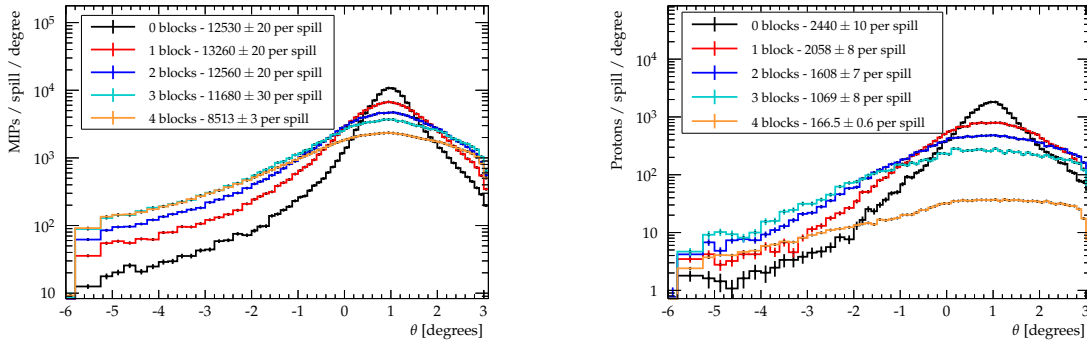


**Figure 24.** Distribution of hits in S3 as a function of the horizontal off-axis angle, measured from S1, for varying numbers of moderator blocks. No coincident hit in S2 was required. Left: minimum ionizing particles. Right: protons. The errors shown in the legend are the statistical error in particle number per spill.

367 The distributions vs. off-axis angle of MIPs and protons in S3 are shown in Figure 24. In both  
 368 cases, the peak beam intensity falls and broadens in  $\theta$  with the increasing number of moderator blocks.  
 369 At off-axis angles the number of MIPs and protons is increased as the number of moderator blocks is  
 370 increased. The TPC lies within this off-axis region. The spread of particles for unmoderated data was  
 371 unexpected; this peak was broadened by the beam steering scattering that led to the double proton  
 372 peaks seen in figures 16 and 17. For the unsteered and unmoderated beam, the measured horizontal  
 373 FWHM is 9.6 cm while the vertical FWHM is 11.0 cm. This is compared with the measured horizontal  
 374 FWHM for the unmoderated and steered beam of 16.8 cm.

375 Figure 25 shows the proton-MIP ratio measured in S3 as a function of the nominal off-axis angle,  
 376 horizontally and vertically respectively, and for various numbers of moderator blocks. For 0, 1, 2, and  
 377 3 moderator blocks the ratio falls to a minimum at approximately  $1^\circ$  with respect to the beam axis.  
 378 This corresponds to the true beam centre for the steered beam. As the angle moves away from the true  
 379 beam centre, the ratio rises for these configurations. The peak of the proton-MIP ratio shifts away from  
 380 the beam centre progressively as more moderator blocks are added (from approximately  $1^\circ$  away from  
 381 beam centre for 0 blocks up to approximately  $3^\circ$  away from beam centre for 3 blocks). At most values  
 382 of  $\theta$ , the proton-MIP ratio falls with the addition of more moderator blocks. Thus, reducing the kinetic  
 383 energy of the protons below 100 MeV came at the cost of reducing the purity of the proton beam.

#### 384 4.2. Flux measurements with S4

385 Figure 26, left, shows the flux of particles identified as minimum ionizing particles across S4. For  
 386 all numbers of moderator blocks, the peak number of minimum ionizing particle events occurs at a  
 387 value of  $\theta$  between  $-1^\circ$  and  $-2^\circ$ . Similarly the number of proton events per spill, shown in Figure 26,

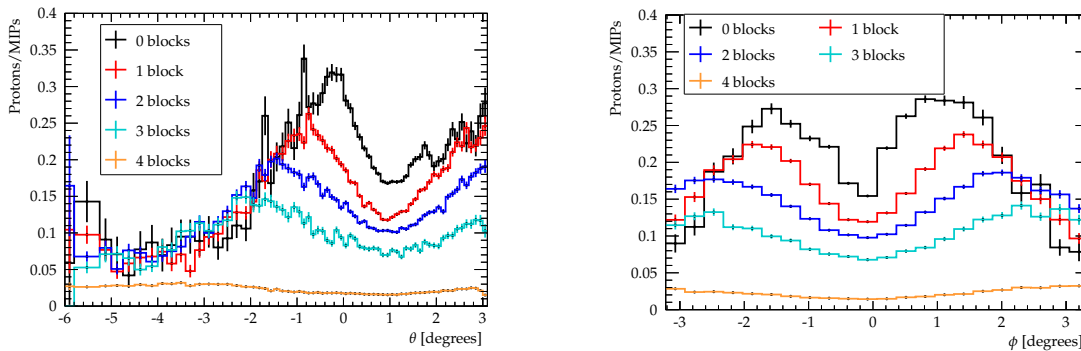


**Figure 25.** Proton-MIP ratio in *S3* for varying numbers of moderator blocks as a function of off-axis angle, as measured from *S1*. Left: horizontal angle. Right: vertical angle. The TPC spans horizontal angles  $1.4\text{--}3.6^\circ$  and vertical angles  $-2.6\text{--}+2.6^\circ$ .

388 right, peaks at a value of  $\theta$  of approximately  $-2^\circ$ . The fall in the number of events between  $\theta = -1^\circ$   
 389 and  $\theta = 0^\circ$  is as a result of the beam impinging on the vessel doors at these angles. The positioning  
 390 and shape of the pressure vessel doors means that, for particles travelling at these angles, a greater  
 391 length of steel is passed through compared to those particles which strike the body of the vessel.

392 Figure 26, left, also shows that initially, an increasing number of moderator blocks results in an  
 393 increased total MIP flux through *S4*. This is because both *S2* and *S4* are positioned off-axis, so the  
 394 unmoderated beam particles do not strike these detectors. Due to scattering processes in the moderator,  
 395 a greater number of MIPs are incident upon *S2* and *S4*, with more scattering occurring with greater  
 396 numbers of moderator blocks. However, with the fourth moderator block the flux of MIPs is seen to  
 397 fall. Similarly, with the addition of the first two moderator blocks, the proton flux shown in Figure 26,  
 398 right, initially sees an increase in the total number of events in *S4*. However, with three and four  
 399 moderator blocks, the total number of protons observed in *S4* falls. The initial proton flux increase is  
 400 similar to that for the MIP flux, with increased scattering causing more protons to pass through the  
 401 off-axis *S2* and *S4* detectors. The subsequent decrease is due to the larger loss of energy of the protons  
 402 in the thicker moderator. In turn, this leads to attenuation of protons in the pressure vessel resulting in  
 403 fewer observed events in *S4*.

404 Figure 27 shows the ratio of protons to MIPs as a function of the number of moderator blocks,  
 405  $\theta$  and  $\phi$ . For all of the different block configurations, the ratio is flat across both  $\theta$  and  $\phi$ . With the  
 406 addition of moderator blocks, the ratio reduces from its highest level of 0.5 for the 0 block case, to  
 407 0.002 for the 4 block data. As mentioned previously, this is thought to be due to the attenuation of low  
 408 energy protons within the walls of the pressure vessel.

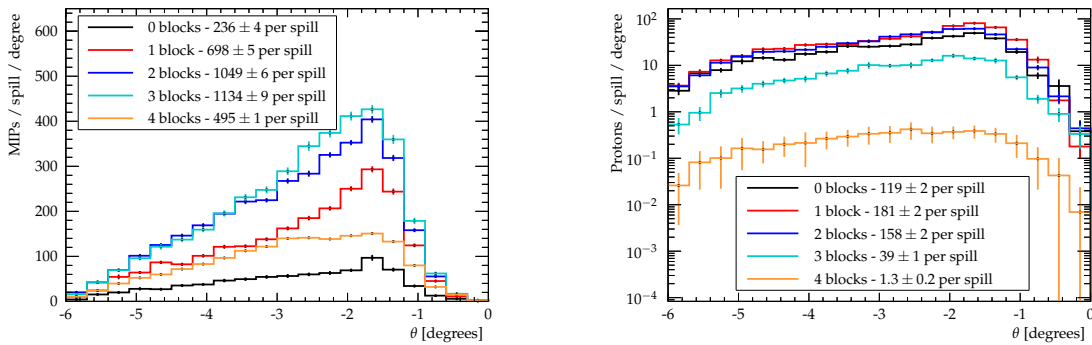


**Figure 26.** Distribution of hits in *S4* as a function of the number of moderator blocks and the horizontal off-axis angle. Left: minimum ionizing particles. Right: protons. The errors shown in the legend are the statistical error in particle number per spill.

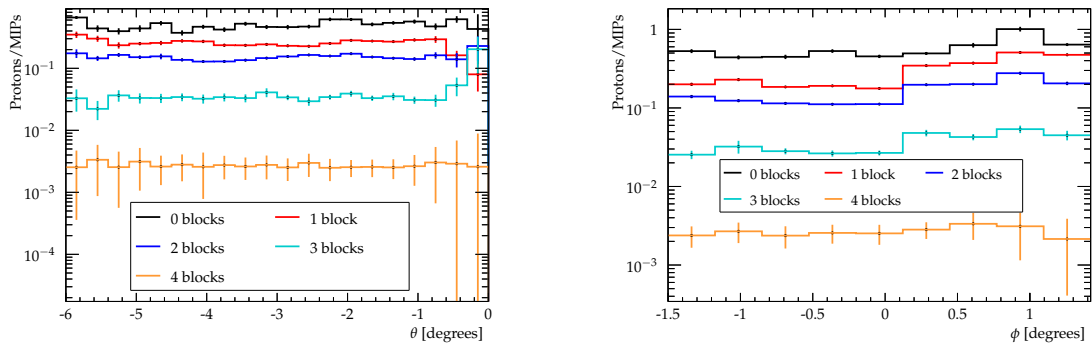


**Figure 27.** Proton-MIP ratio in *S4* for varying numbers of moderator blocks as a function of off-axis angle. Left: horizontal off-axis angle. Right: vertical off-axis angle.

#### 409 4.3. Monte Carlo Studies

410 In order to ascertain the flux of protons reaching the active region of the TPC, and verify the  
 411 corrections described above, a Monte Carlo (MC) simulation study was performed. The simulation  
 412 was performed using GEANT4 [20], with geometric volumes approximating the vessel, TPC, and  
 413 time of flight systems. In order to match upstream conditions as closely as possible, particle momenta  
 414 were drawn from the *S3* distributions shown in Figure 23, left, and simulated with trajectories that  
 415 resulted in the same position distribution as seen in Figure 11, right. The same timing cuts described  
 416 in Section 3.2 were applied.

417 The simulated protons are propagated through the vessel to the *S4* detector. The momentum  
 418 profile of simulated protons reaching the *S4* panel is shown in Figure 28. A proton detection threshold  
 419 of *S4* of 140 MeV/c (10 MeV kinetic energy) is included. The simulation shows a significant reduction  
 420 in kinetic energy as most particles have travelled through both steel walls of the TPC vessel. In  
 421 particular, in the 4 moderator block case, very few particles have survived through the second vessel  
 422 wall to reach *S4*.

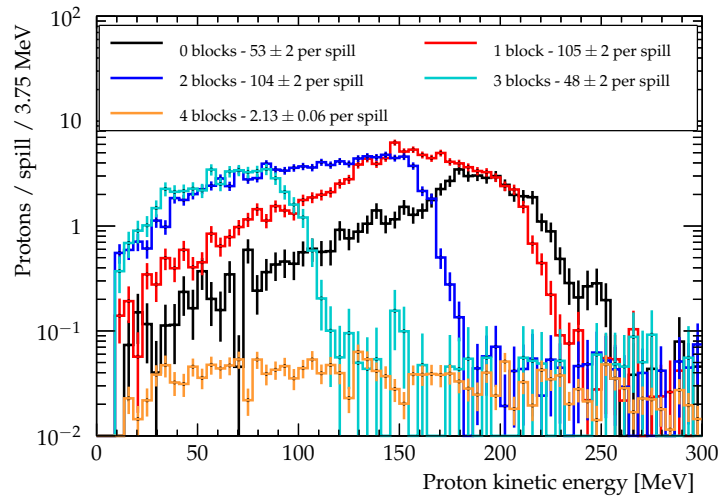


**Figure 28.** Energy profile of simulated protons reaching  $S_4$ , with kinetic energy above the detection threshold of 10 MeV.

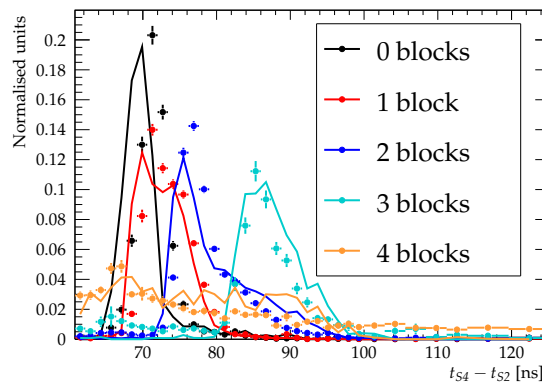


**Figure 29.** Comparison of simulated and measured proton ToF between  $S_2$  and  $S_4$ . Solid lines correspond to the simulated distributions, while points correspond to data. All distributions are area normalised to 1.

423 Comparisons of  $S_2$  to  $S_4$  time of flight for data and MC are shown in Figure 29 for varying  
 424 numbers of moderator blocks. Figure 29 shows that, for all numbers of moderator blocks, the peak  
 425 positions in the data and MC spectra agree to within 2 ns. This level of agreement confirms that the  
 426 simulated energy loss in the vessel and TPC is similar to the energy loss in the data.

427 Systematic uncertainties on the number of protons measured in  $S_3$  and  $S_4$  are estimated for both  
 428 data and MC, and shown in Table 5. The systematic uncertainty on the MC simulation is determined  
 429 by varying the geometric initial conditions of the simulation, including the position of the  $S_1$  and  $S_2$   
 430 detectors. These variations induce changes in the direction and momenta of the propagated protons.  
 431 Additionally, a study was performed with 1 cm of additional acrylic in the beamline, as a proxy for the  
 432 uncertainty on other pieces of light material in the beam facility. This set of calculated errors represents  
 433 geometric sources of uncertainty in the MC simulation.



**Table 5.** List of systematic errors and values for data and MC simulation. All values are the percent error on the  $S4$  proton count with the exception of the uncertainty on the efficiency of  $S3$ , which is the percent error on the  $S3$  proton count. All uncertainties are treated as uncorrelated.  $n_{S4, MC}$  refers to the number of protons reaching  $S4$  in MC simulations.

<b>Monte Carlo</b>					
	Number of moderator blocks				
	0	1	2	3	4
Systematic uncertainty on $n_{S4, MC}$	9.5%	8.0%	8.5%	17.0%	8.0%

<b>Data</b>					
Source of systematic error	Number of moderator blocks				
	0	1	2	3	4
Absolute efficiency of $S3$	1.1%	11.4%	7.0%	11.4%	4.9%
Absolute efficiency of $S4$	11.0%	11.0%	11.0%	11.0%	11.0%
$S4$ angular correction	2.9%	1.5%	6.7%	8.2%	4.1%
$S4$ background uncertainty	0.18%	0.16%	1.1%	1.4%	8.1%
<b>Total</b>	11.5%	16.0%	14.7%	18.3%	18.9%

434 For the data, the uncertainty on the overall efficiency of  $S3$  is calculated by taking the  $\pm 1\sigma$   
 435 uncertainty on the fitted linear relationship between  $S1 \cap S2$  signals in the upstream and downstream  
 436 ToF DAQs (see Section 3.2) and calculating the fractional change this causes in the  $S3$  proton count.

437 The uncertainty on the overall efficiency of  $S4$  is calculated from the calibration tests performed  
 438 on the  $S4$  bars with a  $^{90}\text{Sr}$  source, as discussed in Section 3.2. The overall efficiency factor of 0.8 was  
 439 calculated using data taken with a significantly different readout to that used in the beam test and  
 440 therefore is subject to variation. The spread in maximum bar efficiencies measured in these  $^{90}\text{Sr}$  source  
 441 tests for the various  $S4$  bars is used as the systematic uncertainty on the overall  $S4$  efficiency.

442 The  $S4$  angular correction systematic uncertainty is assessed by varying the number of horizontal  
 443 bins in Figure 21 from 20 to 10 and taking the fractional change in the number of measured  $S4$  protons.

444 The uncertainty on the  $S4$  background subtraction is determined by taking the  $1\sigma$  error on the  
 445 fitted flat background and determining the resulting change in the number of protons. This has a  
 446 larger effect in the 4 block case because of the very small number of protons detected in  $S4$  relative to  
 447 the background.

448 The ratio of number of protons reaching  $S4$  to those reaching  $S3$  is shown for both simulation and  
 449 data in Table 6, which includes the total statistical and systematic error in each case. The agreement  
 450 shown relative to the uncertainty provided by the beam test setup provides strong evidence that  
 451 efficiency corrections described in Section 3.2 are justified.

452 The number of simulated particles that penetrate the active area of the TPC are shown in Figure 30,  
 453 left and right, as a function of momentum and kinetic energy, respectively. Comparing Figure 30,  
 454 right, with the motivation plot shown in Figure 2, it is clear that 4 moderator blocks were required to  
 455 access the momentum region of interest (below 50 MeV). The off-axis and moderator technique were

**Table 6.** Ratio of number of protons reaching *S4* to number protons reaching *S3* for different numbers of moderator blocks in MC and data. In each instance, the combined statistical and systematic errors are shown.

Number of moderator blocks	Monte Carlo	Data	Data/MC
0	$0.027 \pm 0.003$	$0.049 \pm 0.007$	$1.8 \pm 0.3$
1	$0.067 \pm 0.005$	$0.09 \pm 0.01$	$1.3 \pm 0.2$
2	$0.084 \pm 0.007$	$0.10 \pm 0.01$	$1.2 \pm 0.2$
3	$0.06 \pm 0.01$	$0.036 \pm 0.007$	$0.7 \pm 0.2$
4	$0.011 \pm 0.001$	$0.008 \pm 0.001$	$0.7 \pm 0.1$

456 therefore successful in the extent to which the proton energy was lowered. The number of protons  
 457 reaching the active area of the TPC was per spill ( $7.0 \pm 0.1$ ) for 4 moderator blocks, compared with  
 458 ( $12.6 \pm 0.7$ ) per spill without moderation. For 4 moderator blocks, ( $5.6 \pm 0.1$ ) of those protons had  
 459 energies below 100 MeV. These values were calibrated with the full comparison between data and  
 460 simulation.

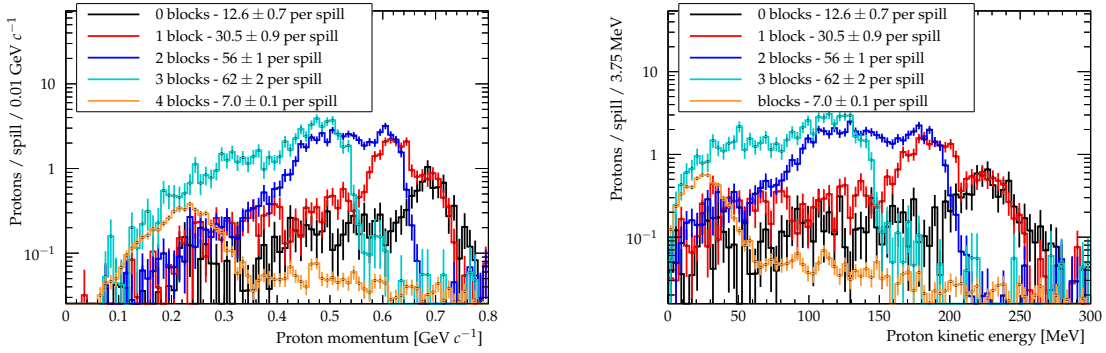


**Figure 30.** Left: Momentum profile of simulated protons reaching the active region of the TPC. Right: Energy profile of simulated protons reaching the active region of the TPC. The errors shown in the legend are the statistical error in particle number per spill.

## 461 5. Conclusion

462 The prototype high pressure gas time projection chamber was operated in the T10 beamline at  
 463 CERN in August and September 2018 in order to make measurement of low momentum protons in  
 464 argon. The vessel was placed at a position off the centre axis of the beam, and a number of acrylic  
 465 blocks were placed directly in the beamline in order to produce a flux of low momentum protons  
 466 through the TPC, ensure a low occupancy of these low energy protons within the TPC and change  
 467 the ratio of MIPs to protons. Measurements of the beam flux were made using two time of flight  
 468 systems placed ( $1.323 \pm 0.001$ ) m upstream and ( $0.918 \pm 0.001$ ) m downstream of the TPC vessel. These  
 469 measurements were used to determine the absolute and relative rates of protons and MIPs as well as  
 470 their momenta, at different positions off the beam axis, and for varying numbers of moderator blocks.

471 When the beam was unsteered, the width was measured to be 9.6 cm. When the beam was steered  
 472 approximately  $1^\circ$  off-axis, the beam width increased to 16.8 cm.

473 These measurements demonstrated that adding moderator blocks reduced the average kinetic  
474 energy of protons reaching the TPC from 0.3 GeV with 0 moderator blocks to 0.1 GeV for 4 moderator  
475 blocks, accessing the kinematic region of interest. This indicates that the off-axis moderator technique  
476 provides a suitable method for providing low energy hadron beams for neutrino detector tests. The  
477 proton/MIP ratio increased at low off-axis angles, peaking at 1–2 degrees off axis, depending on  
478 how many moderator blocks were used, and then fell off at higher angles. The four moderator block  
479 configuration yielded a proton/MIP ratio that was substantially lower than 0–3 blocks and also flat  
480 versus off-axis angle, but achieved the desired proton energy spectrum. With calibration from the  
481 upstream and downstream time of flight systems, for data with 4 moderator blocks in the beamline  
482 the simulated number of protons with energy below 100 MeV reaching the active TPC region was  
483  $(5.6 \pm 0.1)$  per spill with an energy range of 0 to 50 MeV/c.

#### 484 Acknowledgements

485 We wish to acknowledge support for summer students from the Ogden Trust and St. Andrews  
486 University, and outstanding support during the beam test from Johannes Bernhard of CERN as well  
487 as Rebecca Conybeare, Nicole Cullen, Kate Gould, Veera Mikola, Christopher Thorpe, and Simon  
488 Williams.

#### 489 References

- 490
- 491 1. Abe, K.; others. Constraint on the matter–antimatter symmetry-violating phase in neutrino oscillations.  
492 *Nature* **2020**, *580*, 339–344, [[arXiv:hep-ex/1910.03887](https://arxiv.org/abs/1910.03887)]. doi:10.1038/s41586-020-2177-0.
  - 493 2. Mosel, U. Neutrino Interactions with Nucleons and Nuclei: Importance for Long-Baseline  
494 Experiments. *Ann. Rev. Nucl. Part. Sci.* **2016**, *66*, 171–195, [[arXiv:nucl-th/1602.00696](https://arxiv.org/abs/1602.00696)].  
495 doi:10.1146/annurev-nucl-102115-044720.
  - 496 3. Acero, M.; others. First Measurement of Neutrino Oscillation Parameters using Neutrinos  
497 and Antineutrinos by NOvA. *Phys. Rev. Lett.* **2019**, *123*, 151803, [[arXiv:hep-ex/1906.04907](https://arxiv.org/abs/1906.04907)].  
498 doi:10.1103/PhysRevLett.123.151803.
  - 499 4. Abi, B.; Acciarri, R.; Acero, M.A.; Adamov, G.; Adams, D.; Adinolfi, M.; Ahmad, Z.; Ahmed, J.; Alion, T.;  
500 Alonso Monsalve, S.; others. Deep Underground Neutrino Experiment (DUNE), Far Detector Technical  
501 Design Report, Volume II: DUNE Physics, 2020, [[arXiv:hep-ex/2002.03005](https://arxiv.org/abs/2002.03005)].
  - 502 5. Abe, K.; Abe, T.; Aihara, H.; Fukuda, Y.; Hayato, Y.; Huang, K.; Ichikawa, A.; Ikeda, M.; Inoue, K.; Ishino,  
503 H.; others. Letter of Intent: The Hyper-Kamiokande Experiment — Detector Design and Physics Potential  
504 —, 2011, [[arXiv:hep-ex/1109.3262](https://arxiv.org/abs/1109.3262)].
  - 505 6. Acciarri, R.; Acero, M.; Adamowski, M.; Adams, C.; Adamson, P.; Adhikari, S.; Ahmad, Z.; Albright,  
506 C.; Alion, T.; Amador, E.; others. Long-Baseline Neutrino Facility (LBNF) and Deep Underground  
507 Neutrino Experiment (DUNE) Conceptual Design Report, Volume 4 The DUNE Detectors at LBNF, 2016,  
508 [[arXiv:physics.ins-det/1601.02984](https://arxiv.org/abs/1601.02984)].
  - 509 7. Andreopoulos, C.; others. The GENIE Neutrino Monte Carlo Generator. *Nucl. Instrum. Meth.* **2010**,  
510 *A614*, 87–104, [[arXiv:hep-ph/0905.2517](https://arxiv.org/abs/0905.2517)]. doi:10.1016/j.nima.2009.12.009.
  - 511 8. Hayato, Y. A neutrino interaction simulation program library NEUT. *Acta Phys. Polon.* **2009**, *B40*, 2477–2489.

- 512 9. Golan, T.; Sobczyk, J.; Żmuda, J. NuWro: the Wrocław Monte Carlo Generator of Neutrino  
513 Interactions. *Nuclear Physics B - Proceedings Supplements* **2012**, 229-232, 499. Neutrino 2010,  
514 doi:<https://doi.org/10.1016/j.nuclphysbps.2012.09.136>.
- 515 10. Lalakulich, O.; Gallmeister, K.; Mosel, U. Neutrino Nucleus Reactions within the GiBUU Model. *J. Phys.*  
516 *Conf. Ser.* **2013**, 408, 012053, [[arXiv:hep-ph/1110.0674](https://arxiv.org/abs/hep-ph/1110.0674)]. doi:10.1088/1742-6596/408/1/012053.
- 517 11. Carlson, R.F. Proton-Nucleus Total Reaction Cross Sections and Total Cross Sections Up to 1 GeV. *Atom.*  
518 *Data Nucl. Data Tabl.* **1996**, 63, 93–116. doi:10.1006/adnd.1996.0010.
- 519 12. Wellisch, H.; Axen, D. Total reaction cross section calculations in proton-nucleus scattering. *Physical Review*  
520 *C* **1996**, 54, 1329.
- 521 13. Bross, A.; others. High-Pressure Argon gas TPC Option for the DUNE Near Detector. Technical Report  
522 DUNE-doc-6652, FNAL, 2018.
- 523 14. Abe, K.; others. Observation of Electron Neutrino Appearance in a Muon Neutrino Beam. *Phys. Rev. Lett.*  
524 **2014**, 112, 061802, [[arXiv:hep-ex/1311.4750](https://arxiv.org/abs/hep-ex/1311.4750)]. doi:10.1103/PhysRevLett.112.061802.
- 525 15. McFarland, K.S. "Experiment Summary Talk". 12th International Workshop on Neutrino-Nucleus  
526 Scattering in the Few-GeV Region (NuInt18); , 2018.
- 527 16. Coloma, P.; Huber, P. Impact of nuclear effects on the extraction of neutrino oscillation parameters. *Phys.*  
528 *Rev. Lett.* **2013**, 111, 221802, [[arXiv:hep-ph/1307.1243](https://arxiv.org/abs/hep-ph/1307.1243)]. doi:10.1103/PhysRevLett.111.221802.
- 529 17. Raaf, J.; others. DUNE HPgTPC White Paper. forthcoming.
- 530 18. Andreopoulos, C, e.a. Proposal to Measure Hadron Scattering with a Gaseous High Pressure TPC for  
531 Neutrino Oscillation Measurements. Technical Report CERN-SPSC-2017-030. SPSC-P-355, CERN, Geneva,  
532 2017.
- 533 19. Simon, D J, e.a. Secondary beams for tests in the PS East experimental area. Technical Report  
534 PS-PA-EP-Note-88-26, CERN, Geneva, 1988.
- 535 20. Brun, R.; Urban, L.; Carminati, F.; Giani, S.; Maire, M.; McPherson, A.; Bruyant, F.; Patrick, G. GEANT:  
536 detector description and simulation tool. Technical report, CERN, 1993.
- 537 21. *Hamamatsu Photonics K.K.*, (accessed March, 2019). <http://www.hamamatsu.com>.
- 538 22. Korzenev, A.; others. Plastic scintillator detector with the readout based on an array of large-area SiPMs  
539 for the ND280/T2K upgrade and SHiP experiments. International Workshop on New Photon Detectors  
540 (PD18) Tokyo, Japan, November 27-29, 2018, 2019, [[arXiv:physics.ins-det/1901.07785](https://arxiv.org/abs/physics.ins-det/1901.07785)].
- 541 23. *SCIONIX HOLLAND BV, Radiation Detectors & Crystals*, (accessed March, 2019). <http://scionix.nl>.
- 542 24. *Eljen Technology - EJ-200, EJ-204, EJ-208, EJ-212*, (accessed August, 2019). [http://https://](http://https://eljentechnology.com/products/plastic-scintillators/ej-200-ej-204-ej-208-ej-212)  
543 [eljentechnology.com/products/plastic-scintillators/ej-200-ej-204-ej-208-ej-212](http://https://eljentechnology.com/products/plastic-scintillators/ej-200-ej-204-ej-208-ej-212).
- 544 25. Betancourt, C.; others. Application of large area SiPMs for the readout of a plastic  
545 scintillator based timing detector. *JINST* **2017**, 12, P11023, [[arXiv:physics.ins-det/1709.08972](https://arxiv.org/abs/physics.ins-det/1709.08972)].  
546 doi:10.1088/1748-0221/12/11/P11023.
- 547 26. Delagnes, E.; others. The SAMPIC Waveform and Time to Digital Converter. 2014 IEEE Nuclear Science  
548 Symposium (2014 NSS/MIC); , 2014. See Electronique.
- 549 27. *NuviaTech Instruments*, (accessed July, 2019). <http://www.nuviatech-instruments.com>.
- 550 28. Berger, M.; Coursey, J.; Zucker, M.; Chang, J. ESTAR, PSTAR, and ASTAR: Computer Programs for  
551 Calculating Stopping-Power and Range Tables for Electrons, Protons, and Helium Ions (*version 1.2.3*) **2005**.
- 552 29. Deisting, A.; Waldron, A.; others. A High Pressure Time Projection Chamber with Optical Readout. *MDPI*  
553 *instruments*. forthcoming.